UNIVERSITY OF OKLAHOMA
GRADUATE COLLEGE

DESIGN AND SIMULATION OF A RACETRACK PCM-BASED MICRORESONATOR FOR PHOTONIC OPTICAL SWITCHING IN NEUROMORPHIC SYSTEMS

A THESIS
SUBMITTED TO THE GRADUATE FACULTY
in partial fulfillment of the requirements for the
Degree of
MASTER OF SCIENCE

By RAGHD SWEISS

Norman, Oklahoma
2026

DESIGN AND SIMULATION OF A RACETRACK PCM-BASED MICRORESONATOR FOR PHOTONIC OPTICAL SWITCHING IN NEUROMORPHIC SYSTEMS

A THESIS APPROVED FOR THE
SCHOOL OF ELECTRICAL AND COMPUTER ENGINEERING

BY THE COMMITTEE CONSISTING OF

Dr. Sarah Sharif, Chair

Dr. Yaser M. Banad

Dr. Choon Yik Tang

To my parents, Wafaa and Mohammad, whose lives have been shaped by the tragedy of war, yet who never let it define them. They taught me the value of life–to strive for more, to never give in to our circumstances, and to be brave enough to always reach for the stars.

Abstract

Compact and energy-efficient optical switching elements are important for scaling neuromorphic photonic systems and reconfigurable integrated photonics. Resonator-based devices integrated with phase-change materials (PCMs) offer strong light–matter interaction, nonvolatile programmability, and high transmission contrast.

In this work, we study a PCM-integrated silicon racetrack microresonator as a geometry-optimized platform for nonvolatile optical switching, with a focus on material selection and PCM placement. A comparative material study is carried out by introducing a fixed PCM segment at the racetrack waveguide–resonator coupling region and evaluating Sb_2Se_3, Sb_2S_3, and $Ge_2Sb_2Te_5$ (GST) in both amorphous and crystalline states. Using static refractive-index models based on experimentally reported optical constants [1], the materials are compared in terms of transmission contrast, resonance modulation, and linewidth variation. Among the materials considered, GST shows the strongest state-dependent response and is selected for further analysis.

A spatial optimization study is then performed to understand the impact of PCM placement. Four angular positions along the racetrack, separated by 90 degrees, are first evaluated, with the coupling region identified as the most sensitive location. To further improve performance, a finer position sweep is carried out along the straight section of the coupling region, where the GST segment is shifted in 1-µm steps across eight positions. The configuration corresponding to placement P5, located just to the right of the baseline position, produces the highest contrast ratio and modulation depth. This comes at the cost of increased optical loss and reduced resonator quality, highlighting the trade-off between strong modulation and maintaining a high-Q resonance.

All results are obtained using three-dimensional finite-difference time-domain simulations. While dynamic phase-transition effects and power-dependent nonlinearities are not included, the results provide a clear, geometry-driven design framework for PCM-integrated racetrack resonators as nonvolatile optical switches and building blocks for neuromorphic photonic systems. Portions of this work were accepted and presented as an oral paper at SPIE Photonics West 2026 and published in the SPIE Proceedings [2]. The fine-tuning position sweep presented in this thesis extends beyond the published work.

Contents

Abstract **v**

List of Abbreviations **xiii**

1 Introduction **1**

2 Neuromorphic Photonic Computing **4**
- 2.1 Motivation for Neuromorphic Computing 4
- 2.2 Photonic Neuromorphic Hardware: Opportunities and Constraints 5

3 Physics Foundation of Nanophotonic Integrated Design **8**
- 3.1 Electromagnetic Wave 9
- 3.2 Maxwell's Equations 10
- 3.3 Optical Properties of Materials 12
- 3.4 Nanophotonic Integrated Circuits 13
- 3.5 Silicon as the Enabling Platform for Neuromorphic Photonic Hardware 14
- 3.6 Resonant Behavior in Ring and Racetrack Resonators 16
  - 3.6.1 Resonance Condition in Closed-Loop Cavities 16
  - 3.6.2 Whispering Gallery Modes and Field Confinement 16
  - 3.6.3 Mode Overlap and Sensitivity to Localized Index Perturbations 17
  - 3.6.4 Optical Switching Mechanism 18

4 Simulation Domain **20**
- 4.1 Tidy3D Finite-Difference Time-Domain Solver 20
  - 4.1.1 Overview of Tidy3D 20
  - 4.1.2 Cloud-Based Simulation and Workflow 20
  - 4.1.3 Geometric Modeling Capabilities 21
  - 4.1.4 Source Types and Selection Criteria 21
  - 4.1.5 Monitors and Data Extraction 22

4.1.6 Simulation Configuration Parameters 22
4.1.7 Material Modeling 23
4.1.8 Justification for Tidy3D in This Work 23
4.2 Numerical Design Workflow 23
4.3 Simulation Considerations 25

5 Optical Design for Nonvolatile Photonic Switching 26
5.1 Ring Resonator as a Baseline Resonant Building Block 26
5.2 Phase-Change Materials for Nonvolatile Programmability 27
5.3 Racetrack Resonator for Geometry-Driven Switching Optimization 28
5.4 Design Targets and Readout Assumptions for This Thesis 29

6 Optimization of Nonvolatile Photonic Switch 31
6.1 Design Description 31
6.2 Baseline Resonator Response 34
6.3 Material and Location Study Overview 35
6.4 Material Study 36
6.4.1 Evaluation Metrics and Fixed-Wavelength Operation 37
6.4.2 Sb_2S_3-Integrated Racetrack Resonator 37
6.4.3 Sb_2Se_3-Integrated Racetrack Resonator 38
6.4.4 GST-Integrated Racetrack Resonator 39
6.4.5 Material Selection and Design Implications 40
6.5 Location Study 41
6.5.1 Angular Placement Definition and Methodology 41
6.5.2 Switching Response at the Coupling Region (Location 1, 0°) 42
6.5.3 Switching Response Away from the Coupling Region (Locations 2-4) . . . 43
6.5.4 Quantitative Comparison of Switching Metrics 45
6.5.5 Design Implications for Optical Switching 46
6.6 Fine Location Study: High-Resolution Scan Along the Coupling Region 47
6.6.1 Methodology and Placement Definition 48
6.6.2 Evaluation Metrics 48
6.6.3 Physical Interpretation: Why Fine Positioning Matters 49
6.6.4 Results and Design Implications 49
6.7 System-Level Activation Modeling Using a Hybrid Opto-Electronic Approach . . . 54

7 Future Work 58
7.1 Partial Crystallization Modeling 58

7.2 Nonlinearity and Path Toward Nonlinear Optical Switching 59

8 Discussion and Conclusion **61**

References **65**

List of Figures

1.1 Overview of the research progression in this work, from foundational concepts in photonics and phase-change materials to the development of a PCM-integrated racetrack resonator for nonvolatile optical switching, followed by material and location optimization studies. 3

2.1 Conceptual illustration of a PCM-based photonic synapse. A write pulse programs the material state, and a low-power read pulse retrieves the corresponding transmission, enabling state-dependent transmission that can support switching behavior. Adapted from [2]. 6

4.1 Overview of the Tidy3D modeling interface used for the racetrack resonator simulations. Screenshots obtained from the Tidy3D simulation environment developed by Flexcompute [3]. (a) Parameter configuration and project setup within the Tidy3D environment, showing the structure tree, simulation configuration parameters, and material definitions. (b) Geometry selection interface illustrating available photonic components such as straight waveguides, bends, rings, and racetrack structures used to construct the resonator layout. 24

4.2 Source and monitor configuration within Tidy3D. (c) Source selection panel where a guided mode source is chosen to excite the fundamental waveguide mode in the bus waveguide. (d) Monitor configuration interface used to place flux monitors for capturing transmitted optical power and extracting the transmission spectrum used to analyze resonance characteristics. 24

5.1 Nonvolatile optical switching enabled by phase-change materials. Reversible transitions between amorphous and crystalline states modify the complex refractive index, which perturbs the resonator response and produces a state-dependent transmission spectrum. 28

5.2 Schematic of a racetrack resonator coupled to a bus waveguide, highlighting the extended coupling region and distinct geometric sections. The racetrack configuration enables controlled evanescent coupling and provides flexibility in placing localized perturbations, such as PCM segments, for geometry-driven switching optimization. 29

6.1 Geometric design of the silicon racetrack resonator, including the top-view layout and waveguide cross-sectional dimensions. 33
6.2 Baseline Transmission vs Wavelength Graph. 35
6.3 Transmission spectra of the racetrack microresonator integrated with Sb_2S_3 at the coupling region, comparing amorphous and crystalline states under linear optical readout. 38
6.4 Transmission spectra of the racetrack microresonator integrated with Sb_2Se_3 at the coupling region, illustrating phase-dependent resonance shift and linewidth variation. 39
6.5 Transmission spectra of the racetrack microresonator integrated with GST at the coupling region, demonstrating strong state-dependent transmission contrast with minimal resonance distortion. 40
6.6 Definition of GST angular placement locations around the racetrack microresonator. Location 1 corresponds to the waveguide-resonator coupling region (0°). Locations 2-4 are obtained by rotating the same GST segment clockwise by 90° increments (90°, 180°, and 270°). 42
6.7 Transmission spectra of the GST-integrated racetrack microresonator for Location 1 (0°, coupling region). The coupling-region placement yields the largest state-dependent transmission separation and maintains a narrow resonance linewidth under linear readout. 43
6.8 Transmission spectra of the GST-integrated racetrack microresonator for four angular placements of the PCM segment around the resonator perimeter. The strongest state-dependent transmission contrast occurs at the coupling region (Location 1, 0°). As the GST segment moves away from the coupling region (Locations 2–4), the modulation depth decreases and the resonance broadens, indicating reduced modal overlap and weaker linear switching behavior. 44
6.9 Transmission values at $\lambda \approx 1552$ nm for the amorphous and crystalline states of the GST patch at the four angular placements around the racetrack resonator. The coupling-region placement (L1) produces the strongest switching contrast, while placements further from the coupling region show reduced separation between the two states. 46

6.10 Schematic illustration of the fine longitudinal placement scan within the coupling region of the racetrack resonator. The GST patch is translated along the straight coupling section in 1 μm increments to generate candidate positions P1-P8. The previously identified coarse coupling-region placement is marked as the baseline reference location. 48
6.11 Transmission spectra of the GST-integrated racetrack resonator for the first four PCM placements along the coupling region (P1–P4). These positions generally show weaker switching contrast than the baseline, with performance varying non-monotonically along the coupling section. 50
6.12 Transmission spectra for the remaining PCM placements along the coupling region (P5–P8). Among these positions, P5 produces the highest contrast ratio and modulation depth, indicating that this placement lies closest to the locally optimal balance between modal overlap and resonant perturbation. 51
6.13 Comparison of transmission values for amorphous and crystalline GST states at the fixed operating wavelength $\lambda \approx 1552$ nm for the baseline placement and the eight fine-tuned coupling-region positions. The plot highlights the strong spatial sensitivity of switching performance along the coupling section, with placement P5 providing the lowest amorphous-state transmission and the highest contrast ratio. 52
6.14 Linear optical response of the GST-integrated racetrack resonator at the operating wavelength $\lambda \approx 1552$ nm. The output optical power scales linearly with the input optical power, with distinct slopes corresponding to the amorphous and crystalline PCM states. 55
6.15 System-level activation behavior obtained by applying threshold detection to the linear optical response. The amorphous state remains below threshold due to low transmission, while the crystalline state exceeds the threshold at higher input powers, resulting in a binary switching response. 56

List of Tables

6.1 Material study at the coupling region. Switching metrics are evaluated at the amorphous resonance wavelength $\lambda_{a,\min}$. The phase-induced resonance shift is $\Delta\lambda = \lambda_{c,\min} - \lambda_{a,\min}$. 40
6.2 Extracted switching and resonator metrics for the four GST angular placements around the racetrack microresonator. Location 1 corresponds to the waveguide–resonator coupling region (0°). 45
6.3 Extracted switching and resonator metrics for the eight GST placements along the coupling region. 53

List of Abbreviations

AI	Artificial Intelligence
PCM	Phase-Change Material
GST	$Ge_2Sb_2Te_5$
FDTD	Finite-Difference Time-Domain
SOI	Silicon-On-Insulator
TE	Transverse-Electric
TM	Transverse-Magnetic
CR	Contrast Ratio
MD	Modulation Depth
FWHM	Full Width at Half Maximum
Q	Quality Factor

Chapter 1

Introduction

The fast growth of artificial intelligence and neuromorphic computing has increased the demand for hardware capable of high throughput, low latency, and energy-efficient operation. Conventional electronic processors face increasingly significant limitations related to bandwidth, interconnect congestion, and power dissipation, especially in data-intensive and latency-sensitive applications that rely on intensive signal processing, such as optical communications, imaging, and real-time signal processing. Optical computing has emerged as a promising alternative by enabling direct manipulation of optical signals, offering advantages such as large bandwidth, low latency, massive parallelism, and reduced energy consumption [4, 5].

Neuromorphic photonics builds on these advantages by implementing brain-inspired computing architectures using integrated photonic platforms. In photonic neural networks, linear optical components such as interferometers and resonators are typically used to perform weighted summation, while additional device-level or system-level mechanisms are needed to introduce nonlinearity and enable more complex computational behavior [6–8]. A key challenge, therefore, is developing compact, low-power, and scalable photonic building blocks that can support programmable signal modulation and serve as reliable primitives for neuromorphic processing.

Resonant photonic structures, including microring and racetrack microresonators, have been widely studied as compact and energy-efficient elements for optical filtering, modulation, and switching [9–11]. Resonator-based devices enhance light–matter interaction through resonant field buildup, allowing for a smaller footprint and lower operational energy [10]. Racetrack microresonators extend conventional ring geometries by incorporating straight sections, which provide greater control over the coupling region, increase the effective interaction length, and improve sensitivity to localized refractive-index changes [11, 12]. These features make racetrack resonators especially useful for reconfigurable and programmable photonic circuits.

While racetrack microresonators offer strong control over resonance behavior, they remain inherently passive in their standard silicon form. Once fabricated, their transmission response is fixed by geometry and material properties, limiting their ability to support reconfigurable or adaptive functionality. For neuromorphic photonic systems, however, this type of programmability is essential, as weighted operations and activation behavior rely on the ability to modify transmission states in a controlled and persistent manner. Achieving this within a compact resonator structure requires the integration of a material whose optical properties can be reversibly and stably altered.

Phase-change materials (PCMs) provide a practical way to introduce nonvolatile and reversible programmability into integrated photonic devices. Chalcogenide PCMs such as Sb_2Se_3, Sb_2S_3, and GST exhibit large and reversible changes in optical properties between amorphous and crystalline phases, enabling high-contrast modulation without static power consumption [13, 14]. PCM-integrated photonic resonators have been demonstrated as nonvolatile optical switches, tunable resonant devices, and memory elements, making them key building blocks for reconfigurable photonic systems [7, 15, 16].

In neuromorphic and advanced photonic computing architectures, PCM-integrated resonators can act as state-programmable transfer elements, where transmission is set by the material phase and read out using low-power optical signals [15, 17]. Figure 1.1 provides an overview of the research progression in this work, from foundational concepts to device design and optimization of PCM-integrated racetrack resonators for nonvolatile optical switching. The present study focuses specifically on nonvolatile switching through state-dependent transmission. While true optical nonlinearity typically relies on power-dependent material effects or dynamic feedback, static PCM-induced modulation provides a stable and practical foundation for building activation-enabling primitives at both the device and system levels. In this context, optimizing the strength, contrast, and spectral sharpness of state-dependent resonance modulation becomes an important step toward scalable neuromorphic photonic hardware.

Prior work on GST-integrated microring resonators has primarily focused on demonstrating nonvolatile switching and resonance tuning through PCM-induced refractive index changes using fixed material placement along the resonator [11, 18]. However, the influence of PCM material choice and spatial placement on resonance modulation strength and switching performance has received comparatively less attention. This is especially relevant in racetrack geometries, where coupling-region interactions and localized field distributions can significantly impact the overall device response.

In this work, we systematically study a PCM-integrated silicon racetrack microresonator as a geometry-driven platform for nonvolatile resonant optical switching. First, a comparative material study evaluates Sb_2S_3, Sb_2Se_3, and GST integrated at the waveguide–resonator coupling region using experimentally reported optical constants. Based on transmission contrast and resonance modulation, GST is identified as the most effective material. Next, an angular placement study examines the effect of positioning a fixed-size GST segment at four locations along the racetrack resonator. Using three-dimensional finite-difference time-domain simulations, we show that placing GST at the coupling region produces the strongest state-dependent modulation, along with a narrow resonance linewidth and high contrast ratio. This is followed by a fine-tuning study within the coupling region, where the PCM position is incrementally shifted to capture local sensitivity variations and better understand placement-dependent trade-offs.

By isolating both material- and geometry-driven effects, this work establishes practical design guidelines for optimizing PCM-integrated racetrack resonators as nonvolatile optical switches and activation-enabling building blocks for neuromorphic photonic systems. Future extensions that incorporate dynamic phase transitions, multilevel PCM states, or power-dependent effects may further enable fully nonlinear activation behavior.[1]

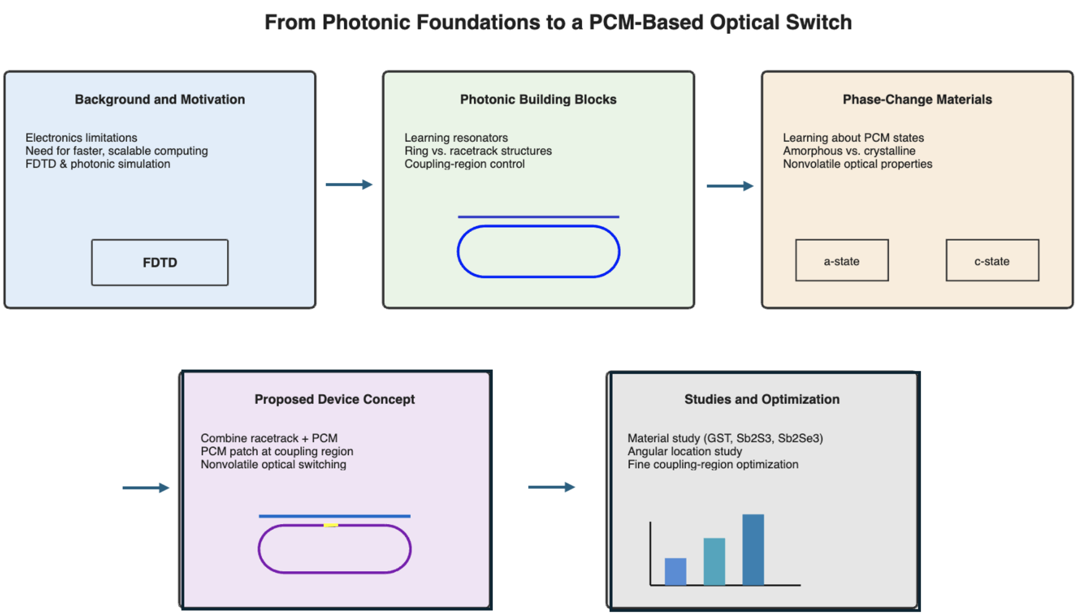

Figure 1.1: Overview of the research progression in this work, from foundational concepts in photonics and phase-change materials to the development of a PCM-integrated racetrack resonator for nonvolatile optical switching, followed by material and location optimization studies.

[1]Portions of this chapter are based on previously published work in: [2].

Chapter 2

Neuromorphic Photonic Computing

2.1 Motivation for Neuromorphic Computing

Artificial intelligence has progressed at an extraordinary pace. Deep neural networks now perform image recognition, language modeling, and decision-making tasks at levels that were difficult to imagine just a decade ago. However, beneath this progress lies a growing architectural problem. Most modern AI systems still run on conventional digital hardware built on the von Neumann architecture, where memory and computation are physically separated. This separation requires data to move continuously between memory and processing units during both training and inference. For large-scale neural networks, that data movement often dominates energy consumption and latency. As emphasized by Marković et al. [19], the cost of memory access increasingly outweighs the cost of arithmetic operations themselves. This phenomenon, commonly referred to as the von Neumann bottleneck, has become one of the central limitations in scaling artificial intelligence systems. As models grow in parameter count and complexity, the bottleneck becomes more severe. Training a neural network involves repeatedly reading large volumes of weights, performing multiply-and-accumulate operations, and writing updated parameters back to memory. Even as transistors keep improving, we are no longer limited by how fast we can compute, but by how efficiently we can move information. The energy disparity between digital hardware and biological intelligence makes this limitation even more striking. The human brain operates at roughly 20 W while performing real-time perception, reasoning, and learning. In contrast, training a state-of-the-art language model can require on the order of 1,000 kWh-highlighting the large energy gap [19]. This difference sheds light on a clear mismatch between the structure of neural algorithms and the hardware used to implement them. Biological neural systems co-locate memory and computation within the same physical substrate. Synapses both store information and participate directly in signal processing, while neurons perform local integration and nonlinear transformation. This spatial integration eliminates large-scale data shuttling and enables massive parallelism. Neural circuits operate asynchronously, in an event-driven manner, leveraging analog dynamics and collective behavior rather than rigid clocked execution. These features allow the brain to achieve remarkable computational efficiency [19]. Reproducing such efficiency with conventional CMOS-based digital logic is challenging. Artificial neurons implemented in standard electronics often require dozens of transistors per unit, limiting density and scalability. Moreover, memory and processing remain physically separated, preserving the very bottleneck neuromorphic systems aim to eliminate. Achieving biological levels of connectivity, adaptability, and energy efficiency therefore requires new device concepts that intrinsically merge memory and computation at the physical level. This realization motivates neuromorphic computing. Rather than simply accelerating digital implementations of neural networks, neuromorphic approaches seek to redesign hardware to better align with neural principles, where information is stored as synaptic weights and processed through weighted signal interactions rather than binary logic. Emerging platforms-including resistive switching devices, phase-change materials, spintronic systems, and photonic architectures-offer promising pathways toward such integration [19]. In particular, photonic neuromorphic systems leverage the inherent parallelism and bandwidth of light for high-speed weighted summation, while phase-change materials provide nonvolatile and reconfigurable synaptic behavior. By using material physics directly for computation, these systems move beyond digital abstraction and toward architectures where memory and processing are physically intertwined. Ultimately, neuromorphic computing arises from a simple but profound observation: computers can be designed to operate more like the brain.

2.2 Photonic Neuromorphic Hardware: Opportunities and Constraints

The architectural limitations of conventional computing discussed in the previous section motivate the search for alternative physical substrates that more naturally support neuromorphic computation. As discussed by Marković et al. [19], future computing systems must move beyond purely digital abstraction and instead leverage intrinsic device physics to co-locate memory and computation. Within this broader context, photonics has emerged as a promising candidate platform for neuromorphic hardware [5, 20]. Integrated photonic systems use wave superposition and interference, enabling linear weighted summation directly through physical propagation. In particular, matrix–vector multiplication-the dominant operation in neural network inference-can be implemented using interferometric meshes or wavelength-division multiplexing architectures, allowing parallel processing at high bandwidth and low latency [20]. Because optical signals avoid many of the resistive and capacitive limitations of electrical interconnects, photonic accelerators offer an attractive pathway for high-throughput and energy-efficient neural computation. Despite these advantages, linear optical circuits alone do not fully realize neuromorphic functionality. Neural networks require both nonlinear activation and persistent state storage. In conventional optical materials, intrinsic nonlinearities are typically weak and require high optical intensities or long interaction lengths to produce substantial modulation [21]. As a result, purely linear photonic networks cannot directly implement activation functions without additional mechanisms. Equally significant is the absence of nonvolatile memory in standard photonic waveguide systems. Unlike biological synapses, which store weights locally, conventional interferometric circuits are stateless: once light exits the device, no persistent modification remains. This mismatch between optical propagation and synaptic storage motivates the integration of materials capable of retaining programmable optical states. PCMs, particularly chalcogenide alloys such as GST, provide this capability. These materials exhibit reversible and nonvolatile transitions between amorphous and crystalline phases, accompanied by substantial changes in refractive index and absorption [13, 22]. When embedded within silicon photonic structures, PCMs enable persistent tuning of optical transmission and phase response without continuous power consumption. Feldmann et al. [7] demonstrated that integrating GST into silicon waveguides allows synaptic weights to be stored and updated directly in the optical domain, effectively combining memory and photonic computation. Phase-change materials can function as programmable photonic synapses, where optical transmission represents the stored synaptic weight. Figure 2.1 illustrates this concept at a system level, where a PCM element functions as a programmable photonic synapse. A write pulse sets the material state, and a low-power read pulse retrieves the corresponding transmission level for downstream processing.

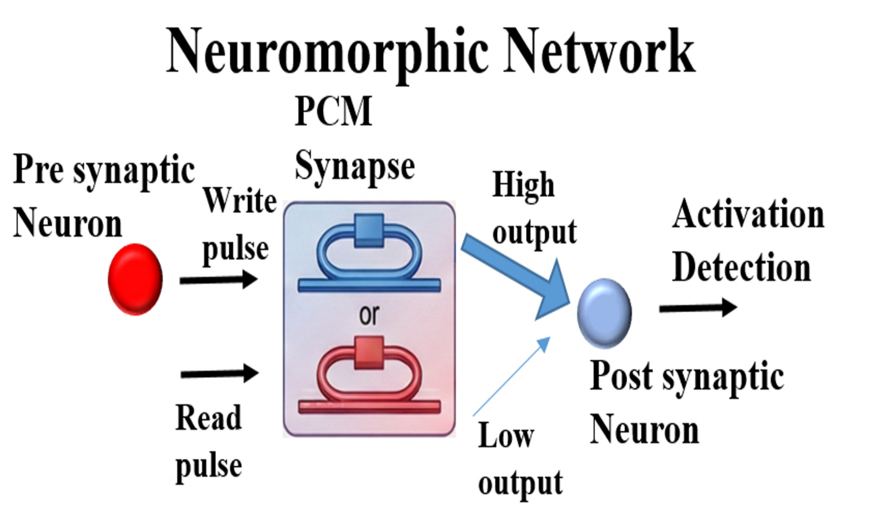

Figure 2.1: Conceptual illustration of a PCM-based photonic synapse. A write pulse programs the material state, and a low-power read pulse retrieves the corresponding transmission, enabling state-dependent transmission that can support switching behavior. Adapted from [2].

Subsequent works have further shown that PCM-integrated microring resonators can realize programmable activation functions with reduced power consumption through resonant field enhancement [10]. Earlier demonstrations of PCM-based racetrack resonators at telecommunications wavelengths established the feasibility of compact nonvolatile optical switching in silicon photonics [11]. Resonant photonic structures play a particularly important role in this context. Optical microcavities confine electromagnetic energy within small modal volumes, increasing light–matter interaction strength and enhancing sensitivity to refractive-index perturbations [9, 23]. This field confinement reduces the energy required to induce measurable transmission changes and enables compact device footprints, making resonators attractive candidates for neuromorphic photonic primitives. Taken together, these developments reveal a central challenge and opportunity in photonic neuromorphic hardware. Linear optical propagation enables efficient parallel weighted summation, yet scalable systems require compact mechanisms for nonlinearity and nonvolatile memory. Phase-change material integration within resonant silicon photonic structures offers a pathway to address both requirements simultaneously. Motivated by these considerations, the present work investigates PCM-integrated silicon racetrack resonators as geometry-sensitive platforms for nonvolatile resonant optical switching. By systematically evaluating material choice and spatial placement-particularly within the coupling region where resonant sensitivity is maximized-this work aims to advance compact photonic building blocks that align device-level physics with neuromorphic computing principles.

Chapter 3

Physics Foundation of Nanophotonic Integrated Design

This chapter establishes the fundamental physical principles underlying the design of nanophotonic devices investigated in this thesis. While Chapter 2 introduced the computational motivation for neuromorphic photonics, the present chapter focuses on the electromagnetic and material foundations that enable such hardware to function.

Integrated photonics refers to the realization of optical components, such as waveguides, resonators, couplers, and modulators, on a single chip-scale platform. By engineering spatial variations in refractive index, electromagnetic waves can be confined, guided, and manipulated in compact geometries, replacing bulky free-space optical assemblies with scalable on-chip structures. Photonic systems enable high-bandwidth and low-latency signal transmission [24].

Among available material platforms, silicon has emerged as the dominant platform for integrated photonics due to its high refractive index contrast, low optical loss in the telecommunications band, and compatibility with mature CMOS fabrication technology [25]. These advantages enable dense integration of resonant structures capable of strong light confinement and enhanced sensitivity to refractive index perturbations.

To understand the operation of such devices, this chapter proceeds from the fundamentals of electromagnetic wave propagation to the material and structural mechanisms that give rise to resonance, field confinement, and optical switching. This framework enables the design and analysis of racetrack resonators studied in later chapters.

3.1 Electromagnetic Wave

All photonic devices, including waveguides, resonators, and integrated optical switches, ultimately operate through the propagation and manipulation of electromagnetic waves. In contrast to electronic circuits, where information is carried by charge transport, photonic systems encode and process information using oscillating electric and magnetic fields. Understanding the behavior of electromagnetic waves is therefore the starting point for analyzing nanophotonic integrated structures [26, 27].

An electromagnetic wave consists of mutually perpendicular electric ($\mathbf{E}$) and magnetic ($\mathbf{H}$) fields that oscillate in time and space while propagating through a medium. In an ideal homogeneous, lossless medium, these fields satisfy the wave equation derived from Maxwell's equations, and the wave propagates with a phase velocity given by [26]

$$v = \frac{c}{n}, \tag{3.1}$$

where c is the speed of light in vacuum and n is the refractive index of the medium. The refractive index characterizes how strongly the medium interacts with the electromagnetic field and determines the wavelength of light within the material according to [27]

$$\lambda_{\text{medium}} = \frac{\lambda_0}{n}, \tag{3.2}$$

where λ_0 is the free-space wavelength.

In integrated photonic platforms such as silicon-on-insulator (SOI), light propagates in confined waveguide geometries rather than in free space. The electromagnetic fields are spatially restricted by refractive index contrast between a high-index core (e.g., silicon) and a lower-index cladding (e.g., silicon dioxide or air). This confinement gives rise to guided modes, stable field distributions that propagate along the waveguide without radiating away [28].

Unlike plane waves in free space, guided modes are characterized by an effective refractive index n_{eff}, which depends on both material properties and the spatial distribution of the electromagnetic field within the waveguide. The propagation constant β of a guided mode is defined as [27]

$$\beta = \frac{2\pi}{\lambda_0} n_{\text{eff}}, \tag{3.3}$$

indicating that phase accumulation in nanophotonic structures is governed not only by intrinsic material refractive index but also by the modal distribution of the electromagnetic field.

This distinction is especially important in high-index-contrast platforms such as silicon photonics. Because a portion of the guided field extends into the surrounding cladding through evanescent decay, any local change in material composition near the waveguide-such as the introduction of a phase-change material-can modify the effective refractive index experienced by the mode [28]. Even small perturbations in n_{eff} can accumulate phase shifts over propagation distance, directly influencing interference and resonance behavior.

Thus, electromagnetic wave propagation in confined geometries forms the fundamental physical mechanism underlying all integrated photonic devices studied in this thesis. The ability to engineer field confinement, phase accumulation, and modal overlap enables wavelength-selective filtering, resonance enhancement, and refractive-index-sensitive switching. In the following section, Maxwell's equations are introduced to provide the rigorous mathematical framework that governs these electromagnetic phenomena in nanophotonic systems.

3.2 Maxwell's Equations

The propagation of electromagnetic waves in photonic structures is highly controlled by Maxwell's equations. These equations describe how electric and magnetic fields evolve in space and time and how they interact with material media. In differential form, Maxwell's equations are given by [26, 27]

$$\nabla \cdot \mathbf{D} = \rho, \tag{3.4}$$

$$\nabla \cdot \mathbf{B} = 0, \tag{3.5}$$

$$\nabla \times \mathbf{E} = -\frac{\partial \mathbf{B}}{\partial t}, \tag{3.6}$$

$$\nabla \times \mathbf{H} = \mathbf{J} + \frac{\partial \mathbf{D}}{\partial t}, \tag{3.7}$$

where $\mathbf{E}$ and $\mathbf{H}$ are the electric and magnetic fields, $\mathbf{D}$ is the electric displacement field, $\mathbf{B}$ is the magnetic flux density, ρ is the free charge density, and $\mathbf{J}$ is the current density.

In dielectric photonic materials operating below carrier excitation regimes, free charges and conduction currents are typically negligible ($\rho \approx 0$, $\mathbf{J} \approx 0$). Under these conditions, the material response is described through the constitutive relations

$$\mathbf{D} = \varepsilon \mathbf{E}, \qquad \mathbf{B} = \mu \mathbf{H}, \tag{3.8}$$

where ε and μ are the permittivity and permeability of the medium, respectively. For non-magnetic materials such as silicon and common dielectric claddings, $\mu \approx \mu_0$, and optical behavior is dominated by spatial variations in permittivity.

By combining Maxwell's curl equations in a source-free, linear, isotropic medium, the electromagnetic wave equation can be derived [26, 28]:

$$\nabla^2 \mathbf{E} - \mu\varepsilon \frac{\partial^2 \mathbf{E}}{\partial t^2} = 0. \tag{3.9}$$

This equation shows that wave propagation is fundamentally determined by the material permittivity ε, which is directly related to the refractive index n through

$$n = \sqrt{\varepsilon_r}, \tag{3.10}$$

where ε_r is the relative permittivity.

In nanophotonic structures, the spatial variation of $\varepsilon(\mathbf{r})$ plays a central role. Waveguides, resonators, and photonic cavities are all formed by engineering spatial permittivity contrasts that confine and manipulate electromagnetic fields. Unlike homogeneous media, integrated photonic devices are characterized by piecewise-constant or spatially varying refractive index distributions. As a result, the electromagnetic field solutions are no longer simple plane waves but guided modes or cavity modes that satisfy Maxwell's equations under specific boundary conditions.

In the frequency domain, assuming harmonic time dependence of the form $e^{-i\omega t}$, Maxwell's equations reduce to the eigenvalue problem

$$\nabla \times \left(\frac{1}{\mu} \nabla \times \mathbf{E} \right) = \omega^2 \varepsilon(\mathbf{r}) \mathbf{E}, \tag{3.11}$$

which forms the mathematical basis for numerical electromagnetic solvers such as the finite-difference time-domain (FDTD) method and eigenmode solvers used throughout this thesis [28].

Equation (3.11) highlights a key principle: electromagnetic behavior in nanophotonic devices is governed by spatial distributions of permittivity. Therefore, any mechanism that modifies $\varepsilon(\mathbf{r})$-such as phase transitions in a phase-change material-directly alters the modal solutions of Maxwell's equations. In resonant structures, these changes manifest as shifts in resonance wavelength, variations in quality factor, or modifications in transmission characteristics.

From a neuromorphic photonics perspective, Maxwell's equations provides the physical framework that underlies analog optical computation. Wave interference, phase accumulation, resonance enhancement, and refractive-index-sensitive modulation are all direct consequences of field solutions to Maxwell's equations in structured dielectric media. Consequently, understanding electromagnetic field behavior is essential for designing photonic hardware capable of performing programmable switching and activation functions.

Having established the fundamental governing equations, the following section examines how material properties influence electromagnetic wave behavior in integrated photonic platforms.

3.3 Optical Properties of Materials

Based on the previous section, it becomes clear that material properties play a central role in determining photonic device behavior. In nanophotonic systems, light–matter interaction is primarily described through the material permittivity, which directly influences refractive index, absorption, dispersion, and phase accumulation [26, 27].

As introduced previously, the electric displacement field relates to the electric field through

$$\mathbf{D} = \varepsilon \mathbf{E}, \tag{3.12}$$

where $\varepsilon = \varepsilon_0 \varepsilon_r$ is the permittivity of the material. The relative permittivity ε_r is generally frequency-dependent and complex at optical frequencies. The refractive index, defined as $n = \sqrt{\varepsilon_r}$, governs phase velocity and resonance behavior. In absorbing materials, the refractive index is more generally expressed as a complex quantity,

$$\tilde{n} = n + i\kappa, \tag{3.13}$$

where n is the real refractive index and κ is the extinction coefficient [27]. The extinction coefficient accounts for optical absorption, and is related to the absorption coefficient α as

$$\alpha = \frac{4\pi\kappa}{\lambda_0}. \tag{3.14}$$

In integrated photonics, both the real and imaginary parts of the refractive index are important. The real part determines phase velocity and resonance conditions, while the imaginary part governs propagation loss and resonance linewidth. Small variations in n shift resonance wavelengths, whereas increases in κ reduce quality factor and transmission contrast.

Material dispersion further complicates optical behavior. Because permittivity varies with frequency, refractive index is wavelength-dependent. This dispersion affects group velocity and phase accumulation in waveguides and resonators [27]. In high-index-contrast platforms such as silicon photonics, even slight changes in refractive index across the telecommunications band can alter resonance spacing and spectral response.

In addition to linear optical properties, materials can exhibit nonlinear polarization responses. In general, the polarization $\mathbf{P}$ of a dielectric can be expressed as a power series in the electric field [21]:

$$\mathbf{P} = \varepsilon_0 \left(\chi^{(1)}\mathbf{E} + \chi^{(2)}\mathbf{E}^2 + \chi^{(3)}\mathbf{E}^3 + \cdots \right), \tag{3.15}$$

where $\chi^{(1)}$ is the linear susceptibility and higher-order susceptibilities describe nonlinear optical effects. In most silicon photonic devices operating under low-power readout conditions, as considered in this work, the dominant contribution is the linear term. Consequently, the refractive index is treated as constant for a given material state.

PCMs, however, introduce a different mechanism for modifying optical properties. Instead of relying on intensity-dependent nonlinearities, PCMs exhibit structural phase transitions between amorphous and crystalline states, each characterized by distinct values of n and κ. These state-dependent optical constants can differ significantly, producing large effective index perturbations when integrated into a photonic structure. Importantly, this change is nonvolatile: once the material phase is set, the refractive index remains stable without continuous power consumption.

In resonator-based devices, even a localized region with modified refractive index alters the effective modal index n_{eff}, thereby shifting resonance conditions. The magnitude of this perturbation depends on both the intrinsic index contrast of the material and the spatial overlap between the guided mode and the modified region. This principle forms the foundation for refractive-index-sensitive modulation and nonvolatile optical switching.

Therefore, understanding the optical properties of materials, specifically permittivity, dispersion, absorption, and state-dependent refractive index variation, is essential for analyzing and optimizing PCM-integrated racetrack resonators. In the following sections, these material-dependent effects are connected to resonant confinement and sensitivity in closed-loop cavities.

3.4 Nanophotonic Integrated Circuits

Nanophotonic integrated circuits (PICs) enable the manipulation of light on a chip-scale platform by engineering spatial variations in refractive index. Rather than relying on bulk optical elements such as lenses or mirrors, integrated photonic systems confine and guide electromagnetic waves using patterned dielectric structures fabricated on semiconductor substrates [24, 27]. This miniaturization enables compact, scalable, and energy-efficient optical signal processing.

The fundamental building block of an integrated photonic circuit is the optical waveguide. A waveguide consists of a high-refractive-index core surrounded by lower-index cladding materials. Light is confined within the core through total internal reflection, forming guided modes that propagate along a defined path. In SOI platforms, a thin silicon layer serves as the guiding core, while silicon dioxide acts as the lower-index cladding. The high refractive index contrast between silicon and silicon dioxide enables strong optical confinement within submicron geometries [24].

By patterning waveguides into different geometries, various optical components can be realized. Straight waveguides transport optical signals, while bends and tapers control routing and modal transitions. Directional couplers enable power splitting and interference. More complex structures, such as microring and racetrack resonators, introduce wavelength-selective behavior through constructive interference of circulating modes [9].

In resonator-based circuits, light coupled from a bus waveguide into a closed-loop cavity circulates multiple times before coupling back out. This repeated interaction enhances phase sensitivity and enables sharp spectral filtering. The resonance condition depends on the effective refractive index and the optical path length of the cavity, making these structures highly sensitive to material perturbations.

Nanophotonic circuits can therefore perform essential optical signal processing functions including filtering, modulation, switching, and wavelength multiplexing. Because these functions are achieved through passive field confinement and interference, they require minimal static power compared to electronic circuits. Furthermore, photonic circuits can operate at terahertz carrier frequencies with bandwidths far exceeding those of conventional electronic interconnects.

In the context of neuromorphic photonic hardware, integrated photonic circuits provide the physical substrate for implementing weighted summation, interference-based computation, and resonant activation behavior. Linear optical transformations can be performed through interference in waveguide networks, while nonlinear or state-dependent modulation can be introduced through material integration. The combination of high-speed optical propagation and compact device geometry makes nanophotonic integrated circuits an attractive platform for scalable neuromorphic systems.

Having established how electromagnetic waves are confined and routed in integrated photonic structures, the following sections focus on the specific device mechanisms-such as optical switching and resonance sensitivity-that enable programmable and nonvolatile photonic functionality.

3.5 Silicon as the Enabling Platform for Neuromorphic Photonic Hardware

Silicon has emerged as the dominant material platform for integrated photonics due to its unique combination of optical, electrical, and technological advantages. While many dielectric materials can guide light, silicon offers a rare convergence of high refractive index contrast, mature fabrication infrastructure, and compatibility with electronic circuitry. These properties make silicon particularly well suited for large-scale, on-chip photonic integration [24, 25].

One of the most important physical advantages of silicon is its high refractive index in the near-infrared telecommunications band ($n \approx 3.48$ at 1550 nm). When combined with a low-index cladding material such as silicon dioxide ($n \approx 1.44$), this large index contrast enables strong optical confinement within submicron waveguide dimensions. Thus, optical modes can be tightly confined to cross-sectional dimensions on the order of a few hundred nanometers, allowing for compact bends, small resonator radii, and dense photonic integration [9]. This high confinement is essential for realizing micron-scale ring and racetrack resonators with well-defined resonant behavior.

Beyond optical confinement, silicon benefits from the vast technological ecosystem developed for complementary metal-oxide-semiconductor (CMOS) electronics. Fabrication processes for silicon devices are highly mature, scalable, and reproducible, enabling wafer-scale manufacturing with nanometer-level precision. This compatibility allows photonic circuits to be fabricated using processes similar to those employed in modern microelectronics, significantly reducing cost and facilitating co-integration with electronic control circuitry [25]. For neuromorphic photonic systems, such co-integration is particularly valuable because optical signal processing can be combined with electronic thresholding, control logic, and memory on the same platform.

Although silicon is an indirect bandgap semiconductor and therefore inefficient as a light emitter, this limitation does not restrain its role as a passive guiding and modulation medium. Silicon exhibits low optical loss in the telecommunications wavelength range and supports several useful physical effects, including the thermo-optic effect and free-carrier dispersion. These mechanisms enable active modulation and tuning when needed, while maintaining low static power consumption in passive operation [24].

In the context of neuromorphic photonic hardware, silicon provides a stable and scalable foundation upon which additional functional materials can be integrated. PCMs, for example, can be deposited or patterned onto silicon waveguides to introduce programmable refractive index perturbations. The high field confinement in silicon enhances the interaction between the guided mode and such materials, increasing sensitivity to local index changes. This property is central to the resonant switching mechanisms investigated in this thesis.

Furthermore, the compact footprint achievable in silicon photonics enables dense networks of resonators and waveguides to be integrated on a single chip. Such density is crucial for implementing parallel photonic processing architectures inspired by biological neural systems, where large numbers of interconnected units are required. As discussed in Chapter 2, neuromorphic computing benefits from distributed processing and co-localized memory. Silicon photonics offers a practical pathway toward realizing these principles in hardware by combining high-speed optical signal propagation with scalable device integration.

For these reasons, silicon serves not merely as a convenient substrate, but as the enabling material platform that makes resonator-based neuromorphic photonic hardware physically realizable. Having established silicon as the foundational medium, the next section examines how resonant behavior in ring and racetrack geometries leverages silicon's high index contrast to produce wavelength-selective and index-sensitive optical responses.

3.6 Resonant Behavior in Ring and Racetrack Resonators

Resonant photonic structures such as microring and racetrack resonators operate based on constructive interference of optical fields circulating within a closed waveguide path. Unlike straight waveguides, which guide light in a single pass, closed-loop cavities allow optical energy to recirculate multiple times, enabling strong field enhancement and wavelength-selective transmission behavior.

3.6.1 Resonance Condition in Closed-Loop Cavities

Resonance occurs when the round-trip optical phase accumulated by the guided mode equals an integer multiple of 2π. For a racetrack resonator, this condition can be expressed as

$$m\lambda = n_{\text{eff}} L_{\text{rt}}, \tag{3.16}$$

where m is the resonance order, λ is the free-space wavelength, n_{eff} is the effective refractive index of the guided mode, and L_{rt} is the total round-trip optical path length including both straight and curved sections.

This relationship shows that the resonance wavelength depends directly on the effective refractive index experienced by the optical mode. Consequently, any perturbation that modifies n_{eff} will shift the resonance position. For small index changes, the first-order resonance shift can be approximated as

$$\Delta\lambda \approx \lambda \frac{\Delta n_{\text{eff}}}{n_{\text{eff}}}, \tag{3.17}$$

where Δn_{eff} represents the change in effective index induced by a material or geometric perturbation.

These two expressions form the theoretical basis for understanding switching and modulation in resonator-based devices.

3.6.2 Whispering Gallery Modes and Field Confinement

The physical mechanism enabling resonance in ring and racetrack resonators is the whispering gallery mode (WGM). In these structures, light is confined near the perimeter of the cavity through total internal reflection, continuously circulating along the curved waveguide boundary. The term "whispering gallery" originates from acoustics, but in optics it describes electromagnetic modes that remain trapped along curved dielectric interfaces.

As discussed by Vahala [23], optical microcavities supporting WGMs can achieve high (Q) factors, meaning that light remains stored in the cavity for many optical cycles before dissipating. The repeated circulation of optical energy enhances light–matter interaction and amplifies the impact of small perturbations. High-Q resonators therefore exhibit strong wavelength selectivity and sharp transmission features.

In silicon ring and racetrack resonators, WGMs typically correspond to (TE) or (TM) guided modes confined within a high-index silicon core surrounded by lower-index cladding. The strong refractive index contrast enables tight optical confinement in micron-scale geometries, making such resonators well suited for dense on-chip integration.

Importantly, the optical field distribution within a WGM is not uniform along the cavity. Field intensity varies spatially, particularly near the waveguide-resonator coupling region. This spatial variation plays a central role in determining how localized material perturbations influence resonance behavior.

3.6.3 Mode Overlap and Sensitivity to Localized Index Perturbations

Because the circulating optical field repeatedly interacts with the same spatial regions, resonators are inherently sensitive to localized refractive index changes. When a perturbation is introduced-such as a PCM segment placed on the resonator-the effective refractive index experienced by the guided mode is modified through evanescent field overlap.

The magnitude of Δn_{eff} depends on two primary factors: the intrinsic refractive index contrast of the perturbing material and the spatial overlap between the optical mode and the perturbation. Even if the perturbing material occupies only a small fraction of the resonator circumference, its influence can be amplified by repeated round-trip interaction of the circulating mode.

Furthermore, due to nonuniform field distribution along the racetrack geometry, identical PCM segments placed at different angular locations can produce significantly different resonance shifts and transmission changes. Regions near the coupling interface often exhibit enhanced sensitivity because perturbations there affect both the round-trip phase and the coupling condition simultaneously.

Under fixed-wavelength operation, resonance shifts described by Eq. (3.17) translate directly into transmission modulation. When the operating wavelength is positioned near the steep slope of a resonance dip, even a small $\Delta\lambda$ can produce a large change in transmitted optical power. This mechanism enables strong state-dependent switching behavior without requiring intrinsic optical nonlinearity.

Together, these principles establish the physical foundation for the material and location optimization studies presented in later chapters. The resonance condition governs wavelength selectivity, whispering gallery confinement enhances light–matter interaction, and localized index perturbations enable controllable transmission modulation-forming the core physics underlying PCM-integrated racetrack resonators for neuromorphic photonic hardware.

3.6.4 Optical Switching Mechanism

The resonant properties described in the previous subsections enable ring and racetrack resonators to function as highly sensitive optical switching elements. Optical switching in resonator-based devices arises from controlled modification of either the round-trip phase condition or the coupling condition, resulting in a measurable change in transmission at a fixed operating wavelength [9, 23].

In a side-coupled resonator configuration, the transmission spectrum exhibits sharp resonance dips corresponding to constructive interference within the cavity. When the effective refractive index of the guided mode is perturbed, the resonance wavelength shifts according to Eq. (3.17). If the input laser wavelength is held constant near the steep slope of a resonance feature, even a small index change can translate into a large variation in transmitted optical power. This slope-dependent transmission modulation forms the basis of resonant optical switching.

Two primary physical mechanisms can induce such refractive index perturbations in silicon photonics: free-carrier dispersion and thermo-optic effects [24]. While these mechanisms enable high-speed modulation, they typically require continuous electrical biasing or thermal power. In contrast, PCMs provide a nonvolatile alternative by exhibiting large, reversible refractive index contrast between amorphous and crystalline phases [22]. When integrated onto a resonator waveguide, a PCM segment locally modifies the effective refractive index experienced by the whispering gallery mode, thereby shifting the resonance condition without requiring sustained power consumption.

From a systems perspective, resonator-based switching can be understood in terms of interference between the directly transmitted field in the bus waveguide and the field coupled into and out of the cavity. At resonance, destructive interference in the through port produces a transmission minimum, while off-resonance constructive interference restores high transmission [9]. Any perturbation that alters the cavity phase or coupling coefficient therefore changes the interference condition and modifies the transmitted intensity.

Importantly, the magnitude of switching depends on the interplay between intrinsic cavity loss, coupling strength, and resonance linewidth. High-quality-factor (Q) resonators exhibit steep spectral slopes and enhanced sensitivity, enabling large transmission modulation for small index perturbations [23]. However, excessive optical loss-such as that introduced by strongly absorbing materials-can broaden the resonance and reduce switching contrast. Optimal device performance therefore requires balancing index contrast and optical absorption.

In the context of neuromorphic photonic hardware, this resonant switching mechanism provides a controllable and energy-efficient method for encoding binary or multilevel states. By selecting an operating wavelength near a resonance slope and integrating a programmable PCM segment, the device can exhibit distinct transmission levels corresponding to different material phases. Each phase remains optically linear for a given state, yet the system exhibits pronounced state-dependent switching behavior.

Thus, optical switching in ring and racetrack resonators arises from the sensitivity of cavity resonance to localized refractive-index perturbations. In resonant photonic structures, phase accumulation along a closed optical path leads to constructive interference at discrete wavelengths. So, even small changes in effective refractive index can produce measurable shifts in resonance condition, enabling highly sensitive optical modulation.

Chapter 4

Simulation Domain

4.1 Tidy3D Finite-Difference Time-Domain Solver

4.1.1 Overview of Tidy3D

All electromagnetic simulations in this thesis were performed using Tidy3D, a high-performance FDTD solver developed by Flexcompute [3]. Tidy3D is a cloud-based electromagnetic simulation platform designed for large-scale nanophotonic and integrated photonic modeling. It implements a time-domain solution of Maxwell's equations on a spatially discretized Yee grid, enabling full-vector modeling of complex three-dimensional optical structures [3].

The FDTD method directly solves the curl form of Maxwell's equations introduced in Chapter 3. By discretizing both space and time, FDTD allows for accurate modeling of broadband responses, resonant structures, material dispersion, and state-dependent refractive index variations.

Tidy3D distinguishes itself from conventional CPU-based solvers through optimized for high-performance cloud-based execution. This architecture enables high-speed simulation of structures spanning many wavelengths while maintaining fine spatial resolution. For integrated photonic resonators such as the racetrack structures investigated in this work, the ability to efficiently model large computational domains with subwavelength mesh resolution is essential for accurately capturing resonance behavior, evanescent coupling, and phase-change-induced perturbations.

4.1.2 Cloud-Based Simulation and Workflow

Tidy3D operates as a cloud-based simulation service. Rather than relying on local computational hardware, simulations are submitted to remote servers optimized for large-scale electromagnetic workloads. This method provides scalability, reduces hardware management overhead, and enables rapid iteration during design optimization.

Simulations in this thesis were constructed programmatically using the Python API provided by Tidy3D. This scripting-based workflow enables precise parametric control of geometry, material assignment, source definition, monitor placement, and simulation configuration. The Python environment was particularly useful for conducting systematic material and location sweeps, where multiple simulations were generated automatically with controlled parameter variations.

4.1.3 Geometric Modeling Capabilities

Tidy3D supports a variety of primitive geometric objects including boxes, cylinders, spheres, and poly-slabs. For photonic integrated circuit design, script-defined structures such as rings, racetrack resonators constructed from primitive geometries, and directional couplers are available. Additionally, geometries may be imported from external layout files in GDSII or STL format, allowing compatibility with standard silicon photonics design workflows.

In this thesis, the racetrack resonator and bus waveguide were defined parametrically using Python-based geometry construction. The phase-change material segments were modeled as rectangular perturbations positioned along the resonator waveguide. This parametric construction enabled precise control of placement, thickness, and overlap relative to the guided optical mode.

4.1.4 Source Types and Selection Criteria

Tidy3D provides multiple excitation source types, including:

- Mode sources
- Gaussian beams
- Plane waves
- Point dipoles
- Total-field/scattered-field (TFSF) sources
- Custom field and current sources

For integrated waveguide-resonator systems, a **mode source** is the most appropriate excitation mechanism. Mode sources launch the fundamental guided eigenmode of a specified waveguide cross-section, ensuring efficient coupling and eliminating unwanted radiation modes. In this work, a fundamental TE-like mode source, defined using the built-in mode solver, was used to excite the straight bus waveguide. The operating wavelength range was centered around 1.55 μm, consistent with standard silicon photonics telecommunications applications.

4.1.5 Monitors and Data Extraction

Tidy3D offers a comprehensive set of monitors for capturing electromagnetic field behavior and spectral response:

- Flux monitors
- Field monitors
- Mode monitors
- Mode solver monitors
- Field projection monitors
- Time-domain monitors

For the racetrack resonator analysis presented in this thesis, the following monitors were used:

- **Flux Monitors**: Positioned along the bus waveguide to compute transmitted optical power and extract transmission spectra. Transmission was computed as the ratio of output flux to input flux.
- **Mode Monitors**: Used to verify that the launched field remained confined to the fundamental guided mode.

Flux monitors were essential for computing transmission as a function of wavelength and for extracting performance metrics such as contrast ratio, modulation depth, full-width at half-maximum (FWHM), and resonance shift.

4.1.6 Simulation Configuration Parameters

Key simulation parameters configured in Tidy3D include:

- Wavelength sweep range (1.54–1.58 μm)
- Simulation domain size and padding
- Mesh resolution (subwavelength discretization), with grid size sufficiently small to resolve the waveguide dimensions and PCM thickness.
- Simulation run time (ensuring field decay for resonator convergence)

A sufficiently fine grid resolution was selected to accurately resolve the high-index-contrast silicon waveguide interfaces and the thin PCM layer. The simulation runtime was chosen to ensure complete decay of transient fields and accurate steady-state spectral extraction.

4.1.7 Material Modeling

Tidy3D supports both nondispersive and dispersive material models. In this thesis, the optical properties of crystalline silicon were modeled using the dispersive material library provided in Tidy3D, while static refractive index models were used for the amorphous and crystalline states of the phase-change material. The PCM refractive index values were derived from experimentally reported optical constants for phase-change materials, as reported in [1]. Because the focus of this work is linear resonant switching under fixed readout conditions, dynamic phase transition modeling was not included in the electromagnetic simulations.

4.1.8 Justification for Tidy3D in This Work

The choice of Tidy3D was motivated by three primary considerations:

1. **Accuracy:** Full-vector 3D FDTD modeling is required to capture evanescent coupling, resonance buildup, and localized PCM perturbations.

2. **Scalability:** The racetrack resonator spans many wavelengths in physical size, necessitating efficient domain handling.

3. **Parametric Optimization:** Material sweeps, angular placement studies, and fine coupling-region scans require repeated simulations with controlled geometry variation.

The combination of cloud-based execution, Python automation, and high-performance FDTD computation enabled systematic optimization of the PCM-integrated racetrack resonator while maintaining accurate electromagnetic modeling.

Overall, Tidy3D provided a robust and scalable platform that provides accurate electromagnetic modeling for investigating geometry-driven and material-driven optimization of nonvolatile resonant switching structures for neuromorphic photonic applications.

4.2 Numerical Design Workflow

Tidy3D Workflow

a) Parameters

b) Geometry Selection

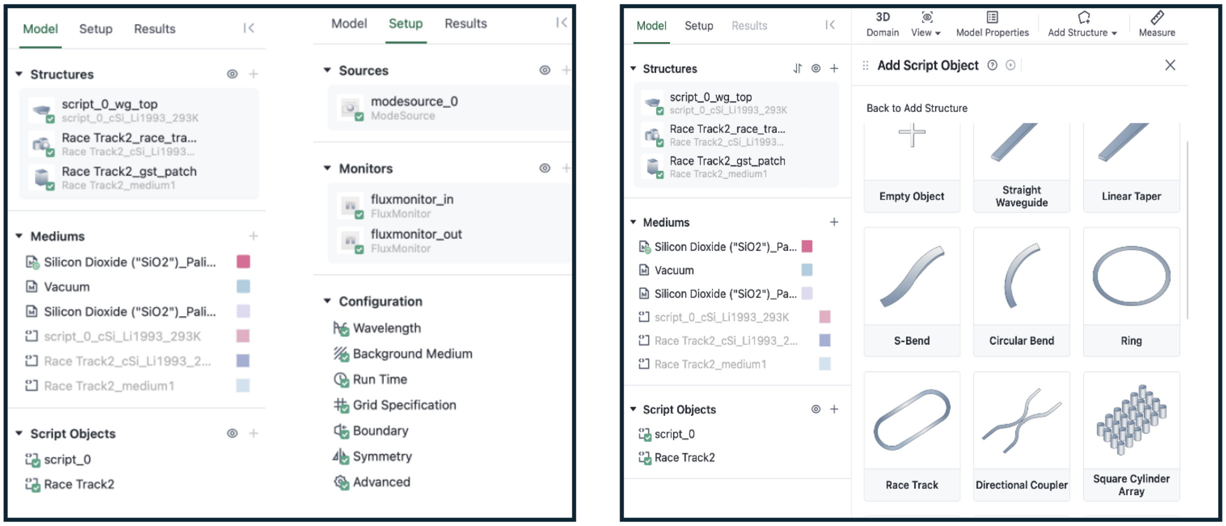

Figure 4.1: Overview of the Tidy3D modeling interface used for the racetrack resonator simulations. Screenshots obtained from the Tidy3D simulation environment developed by Flexcompute [3]. (a) Parameter configuration and project setup within the Tidy3D environment, showing the structure tree, simulation configuration parameters, and material definitions. (b) Geometry selection interface illustrating available photonic components such as straight waveguides, bends, rings, and racetrack structures used to construct the resonator layout.

c) Source Selection

d) Monitor Selection

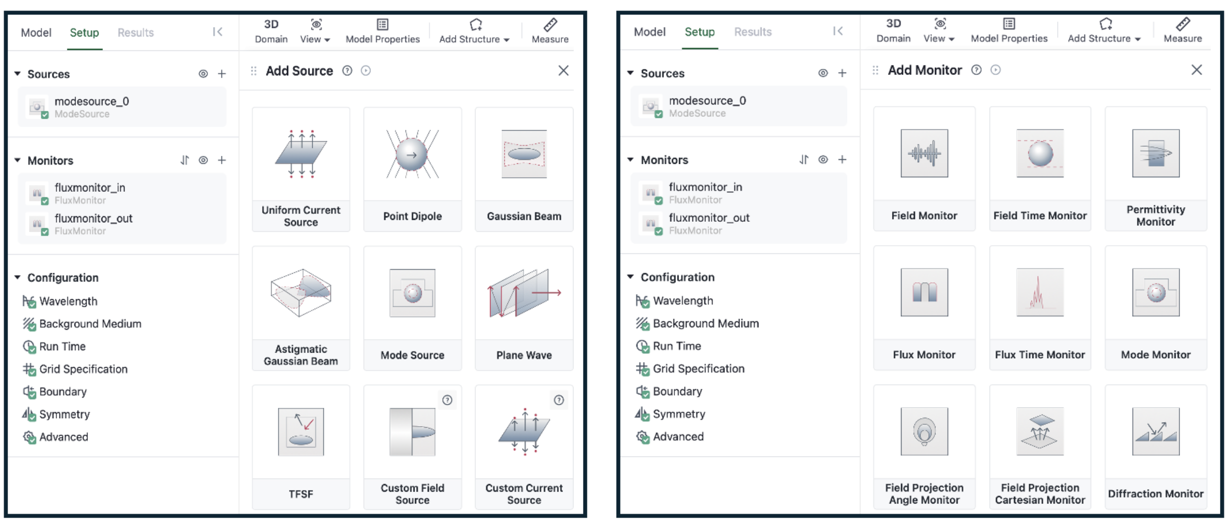

Figure 4.2: Source and monitor configuration within Tidy3D. (c) Source selection panel where a guided mode source is chosen to excite the fundamental waveguide mode in the bus waveguide. (d) Monitor configuration interface used to place flux monitors for capturing transmitted optical power and extracting the transmission spectrum used to analyze resonance characteristics.

4.3 Simulation Considerations

Practical challenges were encountered during the implementation of FDTD simulations in Tidy3D, particularly related to simulation cost, runtime selection, and monitor configuration. Early simulations resulted in high computational cost due to oversized domains, incorrect material parameter units, and inefficient setup. These issues were fixed by reducing the simulation domain, correcting unit definitions, and refining boundary conditions and monitor placement.

Another key challenge was selecting an appropriate simulation runtime. Insufficient runtime led to incomplete field decay, resulting in non-physical artifacts such as oscillations and transmission values exceeding unity, which were attributed to improper normalization and insufficient field decay. This was addressed using the automatic shutoff feature in Tidy3D and by estimating runtime based on the optical travel time across the simulation domain. With these adjustments, the simulations produced stable and physically consistent results.

Chapter 5

Optical Design for Nonvolatile Photonic Switching

This chapter introduces the device-level building blocks used in this thesis and explains why resonator-based structures combined with PCMs provide a practical route toward compact, nonvolatile photonic switching. The emphasis here is not on intrinsic optical nonlinearity, but on *state-programmable* resonant transmission responses that can be read out under low-power, linear operation. This framing is consistent with the system goal explored in later chapters: engineering a racetrack resonator whose transmission spectrum exhibits strong state-dependent contrast and a sharp resonance suitable for fixed-wavelength operation in larger neuromorphic photonic architectures.

5.1 Ring Resonator as a Baseline Resonant Building Block

Ring resonators are widely used in integrated photonics for filtering, modulation, sensing, and wavelength-selective routing. A ring resonator consists of a closed-loop waveguide evanescently coupled to one or more bus waveguides. When the round-trip phase condition is satisfied, optical power builds up in the cavity and produces a wavelength-selective transmission response at the through port (and, in add–drop configurations, at the drop port). Because resonance is determined by the optical path length and the effective refractive index, ring resonators are inherently sensitive to small refractive-index perturbations, enabling compact devices with strong spectral selectivity and high field enhancement [9, 23].

In the context of neuromorphic photonics, this resonant sensitivity is valuable because it allows small, localized changes in material properties to produce measurable changes in transmission. Rather than requiring large device footprints, resonators concentrate optical energy and translate phase perturbations into amplitude changes at the output, which is useful for implementing programmable photonic elements that can act as switching primitives or memory-enabled transfer optical elements in larger systems [9].

Despite their usefulness, conventional circular rings impose geometric constraints that become important when the goal is to *optimize* coupling behavior and study *spatial placement* effects of integrated materials. In a typical microring, coupling occurs over a short curved interaction region, limiting the extent to which coupling strength can be tuned independently from the resonator radius. This can increase sensitivity to fabrication variations and restrict systematic exploration of where an added material (such as a PCM) interacts most strongly with the optical mode. These limitations motivate the use of racetrack resonators, which introduce straight sections that provide additional geometric degrees of freedom while preserving whispering-gallery-type confinement [9].

5.2 Phase-Change Materials for Nonvolatile Programmability

Phase-change materials provide a physically different type of "optical reconfigurability" compared to conventional carrier-based or thermo-optic tuning. Instead of continuously biasing a device to hold a state, a PCM can be reversibly programmed into distinct structural phases (commonly amorphous and crystalline), each with its own complex refractive index. Once programmed, the state is retained without static power, making PCMs attractive for nonvolatile photonic circuits and memory-enabled optical components [13].

A key implication for resonator-based devices is that a PCM segment integrated onto a waveguide can induce a state-dependent change in the effective modal index and loss. In a resonator, these changes can shift the resonance wavelength and modify the resonance depth and linewidth. In practice, this allows a compact device whose transmission spectrum can be *set* by the PCM phase and then *read* using low-power optical probing. As shown in Figure 5.1, transitions between PCM states modify the complex refractive index, which perturbs the resonator response and leads to state-dependent transmission.

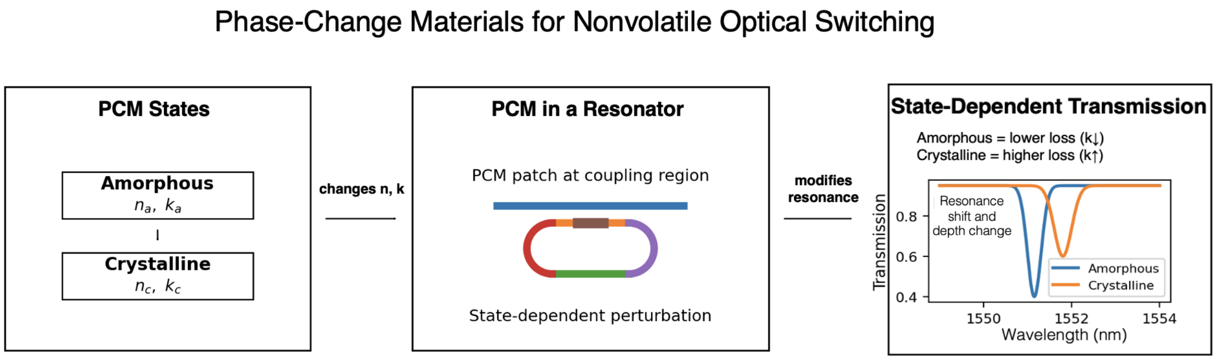

Figure 5.1: Nonvolatile optical switching enabled by phase-change materials. Reversible transitions between amorphous and crystalline states modify the complex refractive index, which perturbs the resonator response and produces a state-dependent transmission spectrum.

Recent experimental work has demonstrated this concept in silicon resonant devices under challenging operating conditions. For example, Adya *et al.* reported non-volatile tuning of silicon photonic micro-ring modulators at cryogenic temperatures using a phase-change layer, showing that resonant states can be programmed and retained without continuous power [29]. Importantly, they also demonstrated multilevel tuning by controlling the programming pulses, which highlights that PCMs can support not only binary switching but also intermediate states, as demonstrated in prior experimental work, when partial phase transitions are used [29]. While the present thesis focuses on linear readout and binary state comparison as a first step, these experimental demonstrations motivate PCMs as a realistic route toward scalable, programmable photonic hardware.

5.3 Racetrack Resonator for Geometry-Driven Switching Optimization

Racetrack resonators extend circular ring geometries by including straight waveguide sections connected by curved bends. This seemingly small change provides substantial design flexibility: the straight sections allow the coupling interaction length to be engineered more directly, enabling stronger and more controllable bus–resonator coupling without requiring extremely small gaps. This is particularly helpful when the design objective is to obtain a sharp resonance (narrow linewidth) while still achieving strong extinction and robust transmission contrast [9].

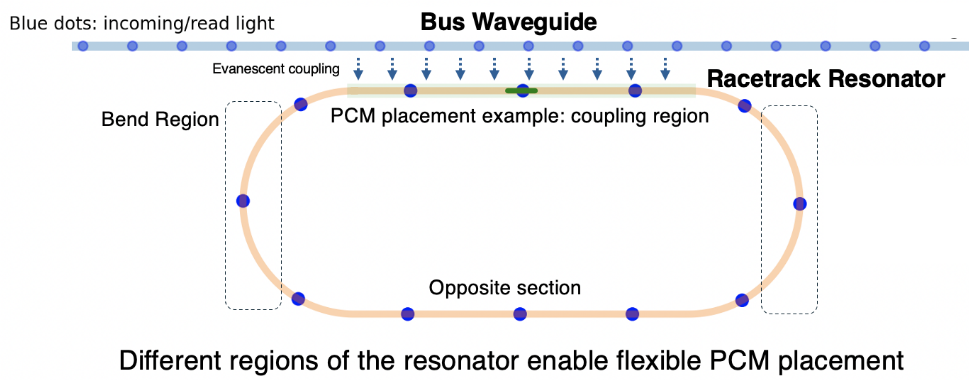

Figure 5.2: Schematic of a racetrack resonator coupled to a bus waveguide, highlighting the extended coupling region and distinct geometric sections. The racetrack configuration enables controlled evanescent coupling and provides flexibility in placing localized perturbations, such as PCM segments, for geometry-driven switching optimization.

In addition to coupling control, racetrack resonators provide a convenient platform for studying *where* a localized material perturbation is most effective. Because the resonator includes distinct functional regions (straight coupling section, bends, and the section opposite the coupler), placing the same PCM segment at different positions can produce meaningfully different effects on the resonance response. In other words, the racetrack geometry makes spatial sensitivity a *design parameter* rather than an uncontrolled artifact. This feature directly supports the methodology used in Chapter 6, where a fixed PCM segment is placed at multiple locations to quantify how geometry and placement affect switching performance.

Finally, racetrack resonators often integrate more naturally into dense layouts because straight sections simplify alignment to buses, allow longer interaction regions, and can accommodate heterogeneous integration elements (such as PCM patches, heaters, or electrodes) with fewer geometric constraints. For these reasons, the racetrack resonator is used in this thesis as the primary device platform for optimizing nonvolatile, resonator-based linear switching.

5.4 Design Targets and Readout Assumptions for This Thesis

To keep the design and evaluation consistent with realistic system operation, this thesis adopts a *fixed-wavelength readout* perspective: the device is assumed to be programmed into a given material state and then probed using a low-power optical signal at a chosen operating wavelength. Under this assumption, the most relevant device-level goals are:

- **Strong state-dependent transmission contrast** between PCM phases at the operating wavelength (useful for reliable readout and switching);

- **Sharp resonance features** (narrow linewidth / high Q factor), which increase slope sensitivity and improve discrimination under fixed-wavelength readout;
- **Controlled loss trade-offs**, since added absorption can broaden resonances and reduce usable contrast even when refractive index contrast is large;
- **Placement-aware optimization**, because the same PCM volume can produce different modulation depending on overlap with the circulating mode and proximity to the coupling interface.

These targets connect the device physics from Chapter 3 to the simulation methodology in Chapter 4 and motivate the systematic material and placement studies presented in Chapter 6.

Chapter 6

Optimization of Nonvolatile Photonic Switch

This chapter extends prior work presented in [2], with additional fine-tuning studies of PCM placement within the coupling region. The first step in the design process was to find the appropriate racetrack parameters to achieve a peak in the transmission vs wavelength graph that is very sharp. This indicates that the sharp resonance improves slope sensitivity and enhances transmission contrast, which is important for fixed-wavelength switching.

The initial geometric parameters were chosen from the default racetrack resonator configuration available in the Tidy3D design environment [3] and then refined through simulation to obtain a narrow, well-defined resonance near the target telecommunications wavelength.

6.1 Design Description

Racetrack Resonator and Bus Waveguide Design Parameters

The photonic structure investigated in this thesis consists of a silicon racetrack resonator side-coupled to a straight bus waveguide, forming an add–drop filter configuration. All geometries were defined parametrically using Python scripts and imported into the electromagnetic solver using a Tidy3D-GDS workflow. The design parameters were selected to ensure single-mode operation near telecommunications wavelengths and to align with commonly reported silicon photonic platforms.

Racetrack Resonator Geometry

The racetrack resonator is centered at (x_0, y_0, z_0) = (0, 0, 0) μm and is composed of two straight waveguide sections connected by semicircular bends. Each bend has a radius of 3 μm, while the straight sections have a length of 8 μm. The silicon waveguide forming the racetrack has a width of 0.52 μm and a thickness of 0.22 μm, which are typical dimensions for silicon-on-insulator (SOI) waveguides operating around 1.55 μm. The sidewall angle is set to zero, corresponding to vertical waveguide sidewalls.

The racetrack geometry is constructed using two separate paths representing the top and bottom halves of the resonator. These paths are converted into three-dimensional structures by extruding the two-dimensional layouts along the vertical direction. The final resonator structure is assigned a crystalline silicon material model based on experimentally measured optical constants.

Bus Waveguide and Coupling Region

A straight bus waveguide is positioned parallel to the top straight section of the racetrack resonator to enable evanescent coupling. The bus waveguide extends from -10 μm to $+10$ μm along the propagation direction and is vertically offset from the resonator to create a nominal coupling gap of approximately 180 nm.

To control the coupling strength between the bus waveguide and the racetrack resonator, the waveguide width is locally modified in the coupling region. Outside the coupling region, the bus waveguide maintains a nominal width of 0.5 μm. Within the coupling region, which spans a length of 4 μm centered at x = 0, the waveguide width is reduced to 0.4 μm. This width reduction enhances modal overlap between the bus waveguide and the resonator, allowing fine control of the coupling coefficient without altering the overall device footprint. Similar coupling strategies have been reported in low-loss SOI racetrack resonators, where narrowing of the waveguide in the coupling region was shown to improve coupling efficiency and quality factor [30].

The bus waveguide thickness is identical to that of the racetrack resonator (0.22 μm), ensuring mode compatibility and efficient coupling. Like the resonator, the bus waveguide is defined using a GDS-based polygonal extrusion and is assigned the same crystalline silicon material properties.

Material Platform

Both the racetrack resonator and the bus waveguide are modeled using crystalline silicon optical properties derived from the Tidy3D design environment. This ensures accurate representation of silicon behavior across the wavelength range of interest. The phase-change material is introduced as an additional structure on top of the resonator. The PCM segment is defined with a length of 0.5 μm, a width matching the waveguide (0.52 μm), and a thickness of 0.05 μm. It is positioned on top of the resonator waveguide. This geometry is kept constant across all materials to isolate material-dependent effects.

Flux Monitor Configuration

To characterize the optical response of the device, frequency-domain flux monitors are placed along the bus waveguide to record transmitted optical power. An input flux monitor is positioned upstream of the coupling region at $(-6, 3.6, 0)$ μm, while an output flux monitor is placed downstream at $(7, 3.6, 0)$ μm. Each monitor has a transverse cross-section of 0.8×0.8 μm^2 to fully capture the guided optical mode.

The transmission spectrum is sampled over a wavelength range from 1.54 μm to 1.58 μm using 2000 frequency points, providing high spectral resolution around the target operating wavelength of 1.55 μm. This configuration enables precise extraction of resonance positions, extinction ratios, and phase-change-induced modulation effects.

Together, these geometric and simulation parameters define a compact, high-index-contrast silicon photonic structure suitable for investigating nonvolatile linear optical switching and state-dependent transmission behavior using PCM resonant devices.

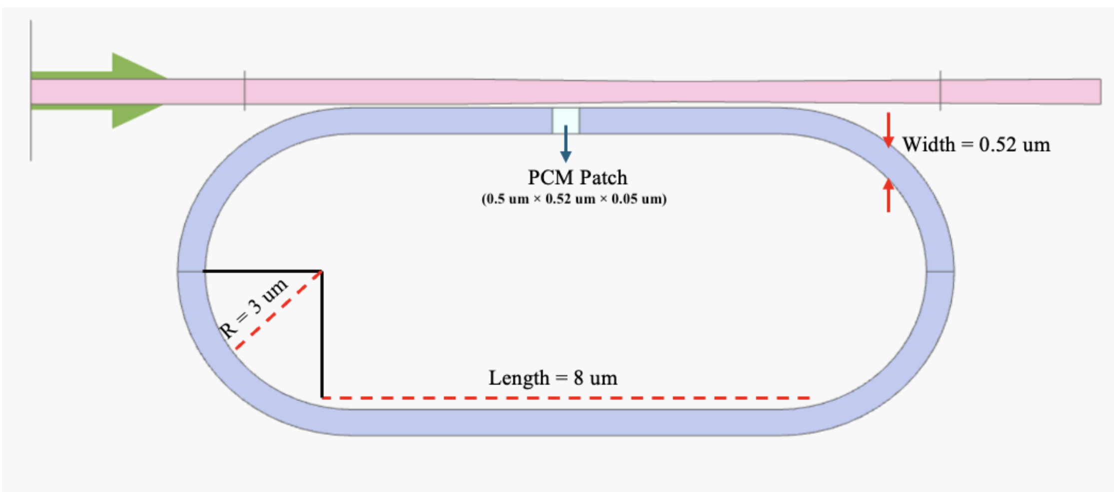

(a) Top view of racetrack resonator.

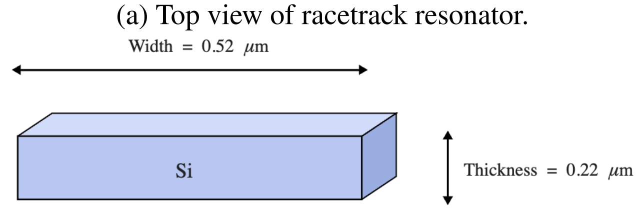

(b) Waveguide cross-section.

Figure 6.1: Geometric design of the silicon racetrack resonator, including the top-view layout and waveguide cross-sectional dimensions.

6.2 Baseline Resonator Response

Before integrating the phase-change material, the intrinsic optical response of the racetrack resonator is first evaluated to establish a reference baseline. This baseline measurement characterizes the resonant behavior of the silicon waveguide structure in the absence of any PCM-induced perturbation. It allows identification of the resonance wavelength, linewidth, and overall transmission characteristics of the device under nominal conditions.

Figure 6.2 shows the transmission spectrum of the baseline racetrack resonator obtained from the simulation. A well-defined resonance dip is observed near $\lambda \approx 1549$ nm, corresponding to the condition where the round-trip optical phase satisfies the resonance condition of the cavity. The sharp spectral feature indicates strong optical confinement within the resonator and efficient coupling with the bus waveguide.

Establishing this baseline response is essential for the subsequent switching analysis. Once the PCM patch is introduced, changes in the effective refractive index of the waveguide alter the resonant condition of the cavity, producing measurable shifts in resonance wavelength and transmission contrast between amorphous and crystalline states. All switching metrics evaluated in later sections are therefore referenced to this baseline resonant behavior.

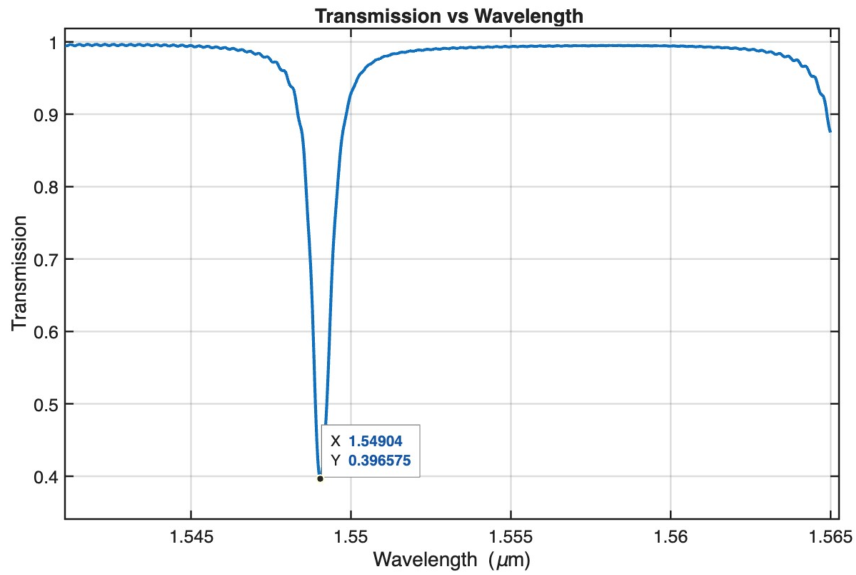

Figure 6.2: Baseline Transmission vs Wavelength Graph.

6.3 Material and Location Study Overview

After establishing the baseline transmission response of the racetrack resonator without any PCM, the device behavior was first analyzed in its purely silicon configuration. This initial step served as a reference case, allowing the intrinsic resonance characteristics of the racetrack-such as resonance wavelength, extinction ratio, and spectral shape-to be identified without perturbations from additional materials. Finding this baseline was essential for isolating the effects introduced by the incorporation of phase-change materials in subsequent simulations.

Following the baseline characterization, a comparative material study was conducted to evaluate the switching performance of different phase-change materials integrated into the resonator. Three candidate materials were considered: GST, Sb_2S_3, and Sb_2Se_3. Each material was introduced into the same racetrack geometry using identical dimensions and placement, ensuring that any observed changes in optical response were attributable to material properties rather than geometric variations. For each PCM, simulations were performed for both low-loss and high-loss optical states corresponding to distinct material phases. The resulting transmission spectra were compared to assess resonance modulation strength, transmission contrast, and overall switching behavior.

The material comparison revealed that GST exhibited the most pronounced optical modulation between its two phases, producing the largest change in transmission at the operating wavelength. In contrast, Sb_2S_3 and Sb_2Se_3 demonstrated more modest variations, resulting in weaker switching behavior under the same conditions. Based on this comparative analysis, GST was selected as the phase-change material for the remainder of the study due to its superior refractive index contrast and stronger influence on the resonator's optical response.

After selecting GST as the optimal PCM, a location study was performed to investigate how the placement of the GST patch along the racetrack resonator affects switching performance. In this study, the GST patch was positioned at four distinct locations around the resonator circumference. The first location was chosen on the straight waveguide section near the coupling region. The remaining three locations were generated by rotating the GST placement clockwise in 90-degree increments around the racetrack, effectively sampling regions of differing modal field distributions.

For each GST placement, transmission spectra were computed for both material phases and compared to evaluate changes in resonance depth, wavelength shift, and modulation contrast. This systematic rotation-based approach identified regions along the resonator where the optical mode exhibits stronger interaction with the GST, thereby enhancing resonant switching behavior. The location study provided insight into the sensitivity of resonator-based switching performance to material placement and informed optimal design choices for neuromorphic photonic applications.

6.4 Material Study

The performance of resonator-based nonvolatile photonic switches is fundamentally governed by the optical contrast introduced by the integrated PCM. In particular, the refractive index difference between the amorphous and crystalline phases of the PCM, as well as the associated optical loss, directly determine the achievable transmission contrast, resonance modulation, and spectral sharpness of the device. In this section, a systematic material study is conducted to evaluate the suitability of different chalcogenide PCMs for linear, nonvolatile resonant switching when integrated into a silicon racetrack microresonator.

Three candidate PCMs are investigated: antimony trisulfide (Sb_2S_3), antimony triselenide (Sb_2Se_3), and germanium antimony telluride ($Ge_2Sb_2Te_5$, GST). These materials were selected due to their relevance in reconfigurable photonics and their distinct optical property changes between amorphous and crystalline phases. In particular, chalcogenide-based PCMs such as GST and Sb-based compounds are widely studied in neuromorphic photonic systems because they exhibit strong, reversible changes in refractive index and absorption while maintaining nonvolatile state retention. GST has been extensively used due to its large optical contrast and fast switching behavior, while Sb_2S_3 and Sb_2Se_3 have emerged as lower-loss alternatives with more moderate index changes, offering a trade-off between modulation strength and optical loss. This range of material properties makes them well-suited for comparative evaluation in resonator-based devices, where both index contrast and absorption critically impact switching performance [31].

To ensure a fair comparison, each PCM is introduced into the same racetrack geometry using identical dimensions and placement at the waveguide–resonator coupling region, where evanescent field overlap and phase sensitivity are strongest. All simulations are performed under identical excitation and boundary conditions using the Tidy3D finite-difference time-domain solver, and the optical response is evaluated under linear readout conditions using static refractive-index models for each material phase.

6.4.1 Evaluation Metrics and Fixed-Wavelength Operation

For neuromorphic photonic systems, practical operation often relies on fixed-wavelength optical sources, where the laser wavelength is not actively tuned during switching. Accordingly, all switching metrics in this study are evaluated at a common operating wavelength defined by the resonance minimum of the amorphous PCM state, denoted $\lambda_{a,\min}$. This approach avoids artificially enhanced performance due to wavelength retuning and reflects realistic system-level constraints.

The switching performance of each PCM is quantified using three key metrics: contrast ratio (CR), modulation depth (MD), and resonance shift $\Delta\lambda$. The contrast ratio is defined as

$$\mathrm{CR} = \frac{T_c(\lambda_{a,\min})}{T_a(\lambda_{a,\min})}, \tag{6.1}$$

where T_a and T_c denote the transmission values in the amorphous and crystalline states, respectively. The modulation depth is given by

$$\mathrm{MD} = \frac{T_c(\lambda_{a,\min}) - T_a(\lambda_{a,\min})}{T_c(\lambda_{a,\min})} \times 100\%. \tag{6.2}$$

Finally, the phase-induced resonance shift $\Delta\lambda$ is extracted as the difference between the resonance minima of the crystalline and amorphous states. Together, these metrics capture the strength, robustness, and spectral stability of PCM-induced linear switching.

6.4.2 Sb_2S_3-Integrated Racetrack Resonator

Figure 6.3 shows the simulated transmission spectra of the racetrack resonator integrated with Sb_2S_3 at the coupling region for both amorphous and crystalline states. The amorphous phase exhibits a moderate resonance dip, while the crystalline phase shows increased transmission at the same wavelength. However, the overall separation between the two states remains limited, resulting in a relatively low contrast ratio and modest modulation depth.

Additionally, Sb_2S_3 introduces a noticeable resonance shift between phases. While this shift indicates phase sensitivity, it reduces effective switching performance under fixed-wavelength operation, as the operating point no longer coincides with the optimal transmission separation. As a result, although Sb_2S_3 demonstrates phase-change-induced modulation, its limited contrast and spectral displacement make it less suitable for robust nonvolatile switching in fixed-wavelength neuromorphic architectures.

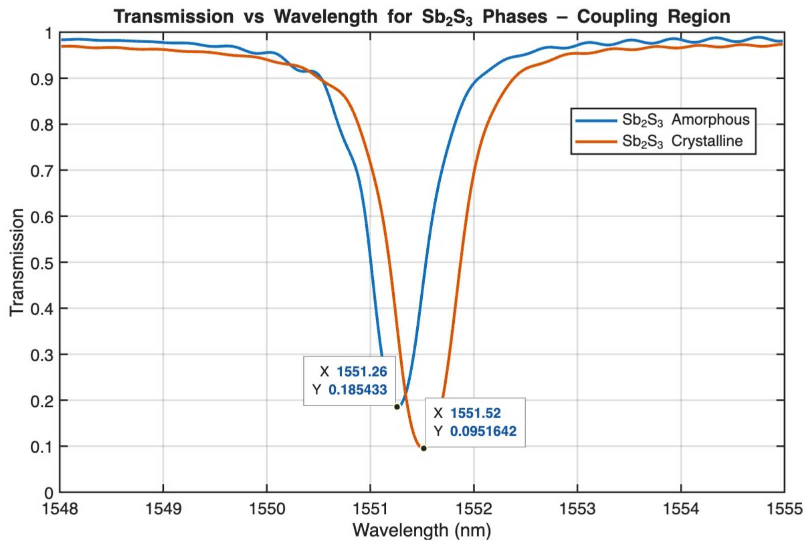

Figure 6.3: Transmission spectra of the racetrack microresonator integrated with Sb_2S_3 at the coupling region, comparing amorphous and crystalline states under linear optical readout.

6.4.3 Sb_2Se_3-Integrated Racetrack Resonator

The transmission response of the Sb_2Se_3-integrated racetrack resonator is shown in Figure 6.4. Compared to Sb_2S_3, Sb_2Se_3 exhibits a larger phase-induced resonance shift, reflecting stronger refractive-index contrast between its amorphous and crystalline states. However, this increased shift is accompanied by linewidth broadening and increased optical loss in the crystalline phase.

As a consequence, while Sb_2Se_3 produces measurable resonance modulation, the effective transmission contrast at the fixed operating wavelength remains limited. The broadened resonance also reduces spectral selectivity, which is undesirable for activation-ready photonic devices that rely on sharp transfer characteristics. These trade-offs highlight the challenge of balancing refractive-index contrast and optical loss in PCM-integrated resonators.

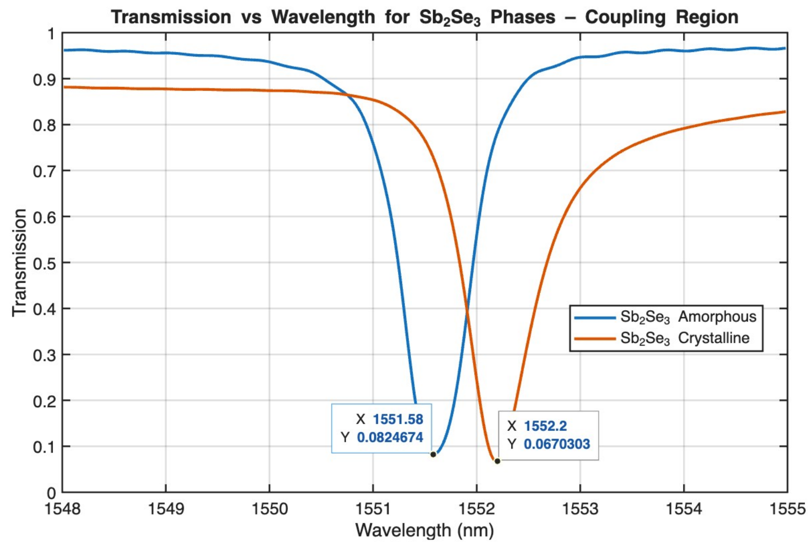

Figure 6.4: Transmission spectra of the racetrack microresonator integrated with Sb_2Se_3 at the coupling region, illustrating phase-dependent resonance shift and linewidth variation.

6.4.4 GST-Integrated Racetrack Resonator

Figure 6.5 presents the transmission spectra for the GST-integrated racetrack resonator at the coupling region. Among the evaluated materials, GST exhibits the most pronounced separation between amorphous and crystalline transmission states at the operating wavelength. The amorphous phase produces a deep resonance dip, while the crystalline phase maintains high transmission with minimal linewidth degradation.

Importantly, GST achieves strong transmission contrast without introducing a significant resonance shift, ensuring that switching performance is preserved under fixed-wavelength operation. This behavior gives the highest contrast ratio and modulation depth among the tested materials, while maintaining a well-defined resonance suitable for resonant activation-enabling behavior. The combination of large state-dependent transmission separation and spectral stability makes GST particularly suitable for nonvolatile linear switching in neuromorphic photonic systems.

To provide a concise comparison of the evaluated phase-change materials, Table 6.1 summarizes the key optical characteristics and switching performance metrics observed for Sb_2S_3, Sb_2Se_3, and GST when integrated at the racetrack coupling region. The comparison highlights clear trade-offs between refractive index contrast, resonance stability, and effective transmission modulation under fixed-wavelength operation.

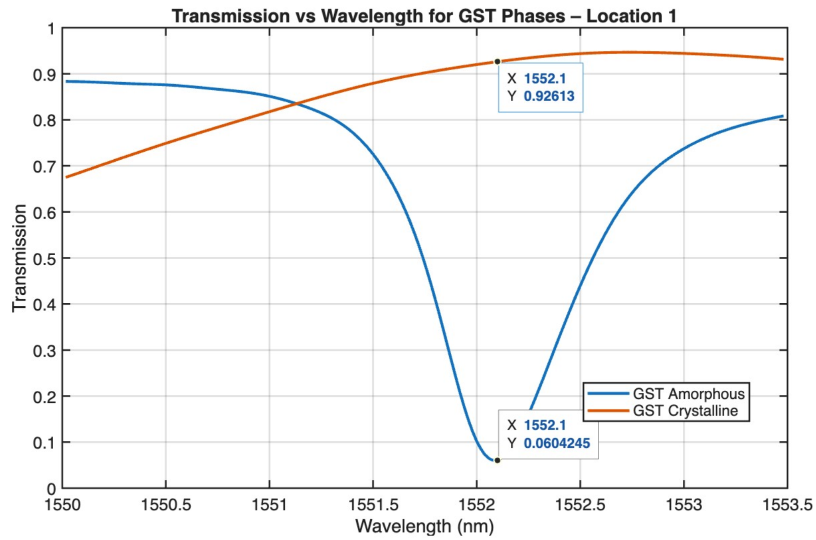

Figure 6.5: Transmission spectra of the racetrack microresonator integrated with GST at the coupling region, demonstrating strong state-dependent transmission contrast with minimal resonance distortion.

Table 6.1: Material study at the coupling region. Switching metrics are evaluated at the amorphous resonance wavelength $\lambda_{a,\min}$. The phase-induced resonance shift is $\Delta\lambda = \lambda_{c,\min} - \lambda_{a,\min}$.

Material	$\lambda_{a,\min}$ (nm)	$T_a(\lambda_{a,\min})$	$T_c(\lambda_{a,\min})$	CR	MD (%)	$\Delta\lambda$ (nm)
Sb_2Se_3	1551.58	0.0825	0.7299	8.8:1	88.70	0.62
Sb_2S_3	1551.26	0.1854	0.3602	1.9:1	48.53	0.26
GST	1552.10	0.0604	0.9261	15.33:1	93.48	< 0.1

6.4.5 Material Selection and Design Implications

A direct comparison across all three materials reveals that GST consistently outperforms Sb_2S_3 and Sb_2Se_3 in terms of contrast ratio, modulation depth, and robustness under fixed-wavelength operation. While antimony-based PCMs show measurable phase-induced modulation, their larger resonance shifts and increased linewidth broadening limit effective switching contrast without active wavelength control.

Based on this comparative analysis, GST is selected as the phase-change material for subsequent optimization studies in this thesis. Its favorable balance of refractive-index contrast, optical loss, and spectral stability enables strong nonvolatile linear switching while preserving the sharp resonance features required for activation-ready photonic transfer functions. Having established GST as the optimal PCM, the following section investigates how the spatial placement of the GST segment around the racetrack resonator can be exploited to further enhance switching performance through geometry-driven optimization.

6.5 Location Study

Following the material study, GST was selected as the phase-change material for placement optimization due to its better state-dependent transmission separation under fixed-wavelength operation. With the material fixed, the next design degree of freedom is *where* the PCM segment is placed along the resonator. In racetrack microresonators, optical field intensity, phase sensitivity, and coupling dynamics vary spatially along the resonator perimeter, with particularly strong sensitivity expected near the waveguide–resonator coupling interface. The objective of this location study is to quantify how the angular placement of a fixed-size GST segment around the racetrack influences state-dependent modulation, resonance sharpness, and overall linear switching performance.

6.5.1 Angular Placement Definition and Methodology

A single GST segment with fixed dimensions and identical optical properties is positioned at four angular locations around the racetrack resonator, separated by 90°. Location 1 corresponds to the waveguide-racetrack coupling region (defined here as 0°), where evanescent interaction and phase sensitivity are strongest. Locations 2-4 are generated by rotating the GST segment clockwise along the racetrack perimeter, placing it progressively farther from the coupling interface at 90°, 180°, and 270°, respectively. All simulations are performed under identical geometry, excitation, and linear optical readout conditions. The amorphous and crystalline GST states are modeled using static refractive indices, meaning that the observed switching behavior arises solely from state-dependent refractive-index perturbations rather than dynamic or power-dependent nonlinear effects.

Figure 6.6 illustrates the four GST placement locations used in this study. This visualization is included to emphasize that the only variable between cases is the spatial overlap between the guided optical mode and the GST segment, enabling a direct geometry-driven comparison.

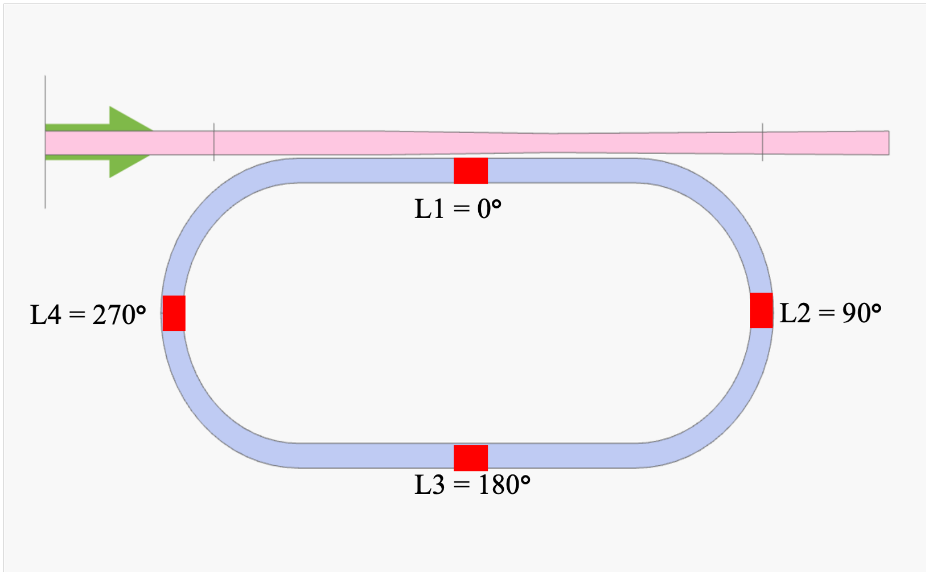

Figure 6.6: Definition of GST angular placement locations around the racetrack microresonator. Location 1 corresponds to the waveguide-resonator coupling region (0°). Locations 2-4 are obtained by rotating the same GST segment clockwise by 90° increments (90°, 180°, and 270°).

6.5.2 Switching Response at the Coupling Region (Location 1, 0°)

Figure 6.7 shows the transmission spectra for GST placed at the coupling region (Location 1) in both amorphous and crystalline states. This configuration shows the strongest linear switching behavior among all tested placements. The amorphous state produces a deep resonance dip, while the crystalline state maintains high transmission at the same operating wavelength, resulting in a large separation between the two transmission states. In addition to strong transmission separation, the resonance linewidth remains narrow, indicating minimal degradation of spectral selectivity. This combination of (i) high state-dependent separation and (ii) sharp resonant behavior is critical for neuromorphic photonic architectures where switching elements must support reliable readout and tight spectral filtering within dense photonic circuits. Physically, the enhanced sensitivity at Location 1 is attributed to strong evanescent field overlap and increased phase sensitivity inherent to the coupling region. In a side-coupled racetrack, small refractive-index perturbations near this interface can strongly impact the effective coupling condition and the round-trip resonant phase, amplifying the impact of the PCM relative to placements where the optical field interaction is weaker.

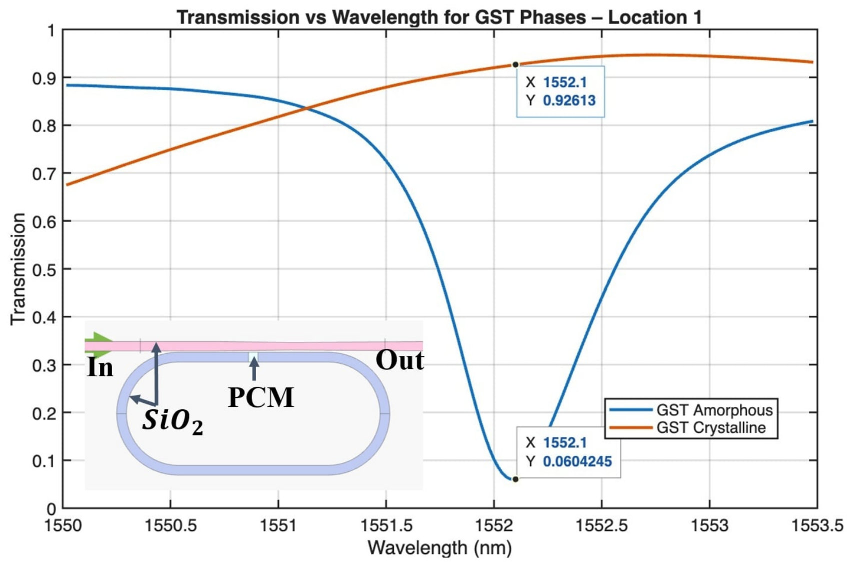

Figure 6.7: Transmission spectra of the GST-integrated racetrack microresonator for Location 1 (0°, coupling region). The coupling-region placement yields the largest state-dependent transmission separation and maintains a narrow resonance linewidth under linear readout.

6.5.3 Switching Response Away from the Coupling Region (Locations 2-4)

Figures 6.8b–6.8d present the transmission spectra for GST placed at Locations 2-4 (90°, 180°, and 270°). As the GST segment is moved away from the coupling region, the state-dependent transmission contrast decreases and the resonance becomes broader. Although the amorphous state continues to show a resonance dip, the crystalline state shows reduced modulation, leading to lower contrast and weaker switching behavior compared to Location 1.

This degradation is consistent with the reduced interaction between the guided optical mode and the PCM segment at locations where optical field intensity and phase sensitivity are lower. In practical terms, these placements reduce the effective perturbation imposed by the PCM on the resonant condition, thereby reducing the difference between amorphous and crystalline transmission states at a fixed operating wavelength.

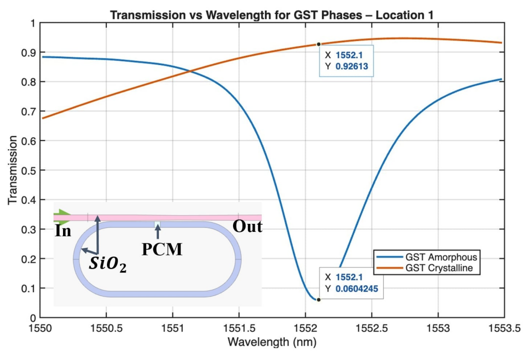

(a) Location 1 (0°) - Coupling region

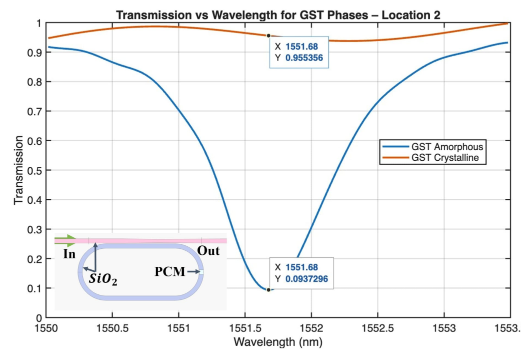

(b) Location 2 (90°)

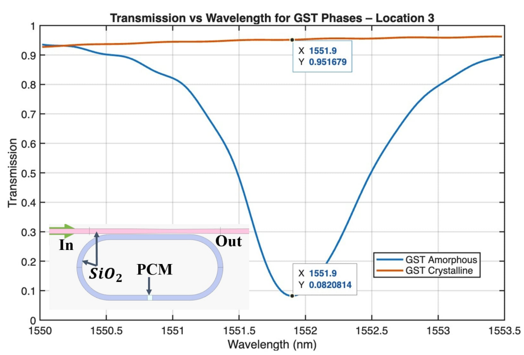

(c) Location 3 (180°)

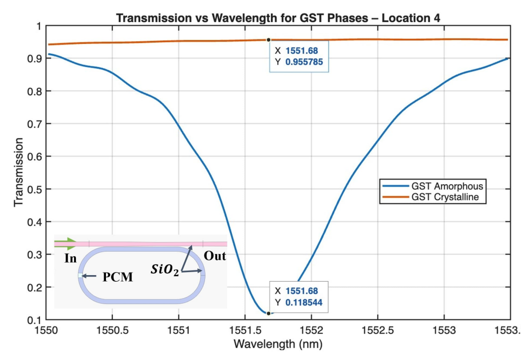

(d) Location 4 (270°)

Figure 6.8: Transmission spectra of the GST-integrated racetrack microresonator for four angular placements of the PCM segment around the resonator perimeter. The strongest state-dependent transmission contrast occurs at the coupling region (Location 1, 0°). As the GST segment moves away from the coupling region (Locations 2–4), the modulation depth decreases and the resonance broadens, indicating reduced modal overlap and weaker linear switching behavior.

6.5.4 Quantitative Comparison of Switching Metrics

To quantitatively evaluate the impact of angular placement, standard resonator and switching metrics are extracted from the transmission spectra, including the FWHM, CR, MD, and Q. Table 6.2 summarizes the extracted metrics across the four locations. The coupling-region placement (Location 1) achieves the narrowest linewidth (FWHM = 0.42 nm), highest contrast ratio (CR = 15.3:1), largest modulation depth (MD = 93.5%), and highest quality factor (Q = 3695.5). In contrast, Locations 2–4 exhibit broader resonances and reduced contrast, confirming that placement away from the coupling region degrades linear switching performance. As further illustrated in Fig. 6.9, the separation between the amorphous and crystalline transmission states is largest at Location 1 and gradually decreases for the other angular placements.

Table 6.2: Extracted switching and resonator metrics for the four GST angular placements around the racetrack microresonator. Location 1 corresponds to the waveguide–resonator coupling region (0°).

Location	**Angle**	**FWHM (nm)**	**CR**	**MD (%)**	**Q**
L1	0°	0.42	15.3:1	93.5	3695.5
L2	90°	0.60	10.2:1	90.2	2586.1
L3	180°	0.66	11.6:1	91.4	2351.4
L4	270°	0.68	8.1:1	87.6	2281.9

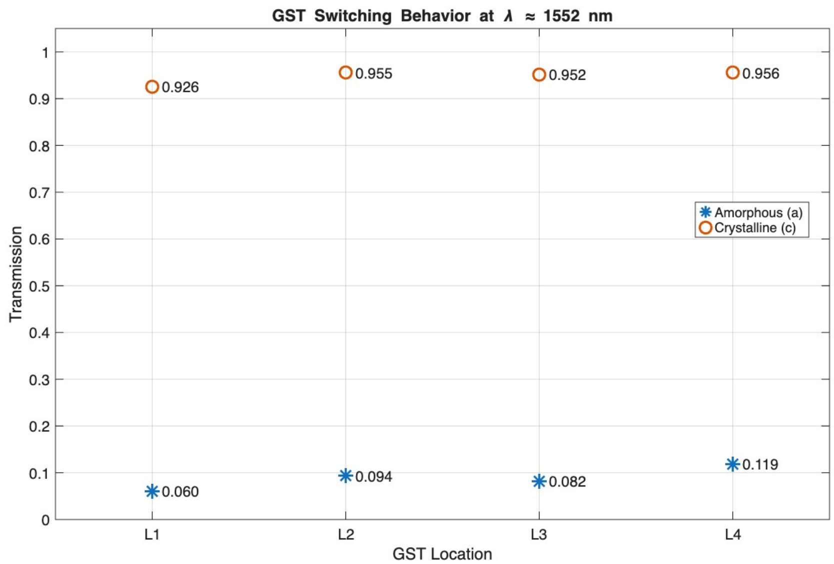

Figure 6.9: Transmission values at $\lambda \approx 1552$ nm for the amorphous and crystalline states of the GST patch at the four angular placements around the racetrack resonator. The coupling-region placement (L1) produces the strongest switching contrast, while placements further from the coupling region show reduced separation between the two states.

6.5.5 Design Implications for Optical Switching

The location study reveals a clear dependence of linear switching performance on GST placement, with coupling-region placement consistently delivering the highest contrast ratio, largest modulation depth, and narrowest linewidth among all tested configurations.

This result shows that placing the PCM at the coupling interface maximizes state-dependent modulation due to two key physical mechanisms. First, the PCM directly modifies the evanescent coupling between the bus and resonator waveguides. The coupling coefficient κ depends on the local refractive index, modal overlap, and waveguide separation. When the PCM is placed at the coupling interface and changes phase state, it alters the refractive index at this critical region, thereby modifying κ and affecting both the coupled power and the resonance quality factor.

Second, the coupling region corresponds to a location of strong optical field interaction and high phase sensitivity. From the resonance condition $m\lambda = n_{\text{eff}} L_{\text{rt}}$, a PCM-induced change in effective index produces a resonance shift. When this perturbation occurs at the coupling interface, where field overlap is strongest, the resulting change in round-trip phase is maximized, leading to stronger transmission modulation at a fixed operating wavelength.

The improvement is therefore achieved through purely geometric optimization, without increasing device footprint or changing material composition.

From a neuromorphic photonics perspective, this result is important for two reasons. First, the large separation between amorphous and crystalline transmission states supports robust binary (or multi-state) readout when the device is used as a nonvolatile switching primitive. Second, maintaining a narrow resonance linewidth preserves spectral selectivity, which is essential in resonator-based photonic systems where multiple elements may be wavelength-multiplexed or cascaded. Together, these features support the use of coupling-region GST placement as an optimal configuration for resonator-based switching elements.

Thus, the location study establishes angular PCM placement as a key design parameter: even with identical PCM volume and identical resonator geometry, switching performance varies substantially depending on where the PCM is placed. These findings motivate the selection of Location 1 (coupling-region placement) as the baseline configuration for subsequent device optimization and for integration into system-level neuromorphic architectures.[1]

6.6 Fine Location Study: High-Resolution Scan Along the Coupling Region

The angular location study in Section 6.5 identified the waveguide–resonator coupling region (Location 1) as the most sensitive placement for GST integration, producing the strongest state-dependent transmission contrast and the sharpest resonance response due to its strong influence on both coupling and phase sensitivity. While this result establishes the coupling interface as the optimal *region* on the racetrack perimeter, the coupling section itself is spatially extended and does not support uniform modal overlap along its length. Due to interference of the resonant light circulating in the cavity and the gradual evanescent coupling between the bus waveguide and the racetrack, the optical intensity varies along the straight coupling section. As a result, some positions along this segment experience stronger optical fields than others, creating local regions where the device becomes more sensitive to refractive-index perturbations. Consequently, the precise longitudinal position of the GST patch along the coupling straight section can further influence the effective index perturbation, resonance modulation strength, and fixed-wavelength switching performance.

To capture this fine-scale sensitivity, an additional optimization study was conducted in which the GST patch was placed along the straight portion of the coupling region and evaluated at eight distinct longitudinal positions. This high-resolution scan aims to identify a placement that maximizes modulation depth and contrast ratio while preserving narrow linewidth and minimal spectral distortion. The sensitivity of different PCM placements arises from variations in the spatial overlap between the guided optical mode and the PCM region along the racetrack waveguide.

[1] Parts of this chapter are based on work previously published in: [2].

6.6.1 Methodology and Placement Definition

A single GST segment with fixed dimensions (identical thickness, length, and width) was placed on the racetrack waveguide within the straight coupling section, maintaining the same coupling gap and the same bus-waveguide geometry as defined in Section 6.4. The patch was then translated along the propagation direction of the bus waveguide to generate eight discrete placements, denoted P_1 through P_8, spanning the entire coupling length. The center-to-center spacing between adjacent placements was chosen to uniformly sample the coupling section, ensuring that the scan resolves local sensitivity variations without altering the device footprint.

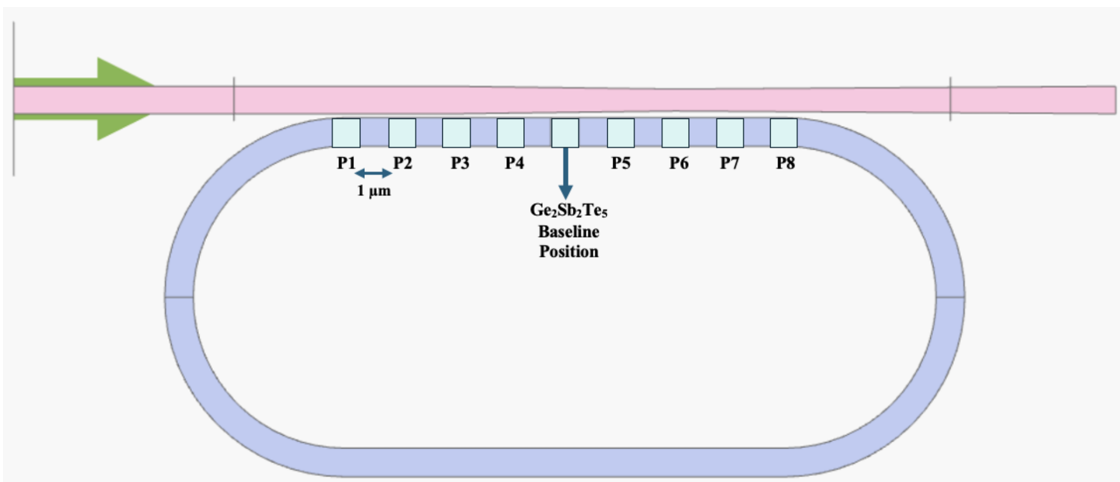

Figure 6.10: Schematic illustration of the fine longitudinal placement scan within the coupling region of the racetrack resonator. The GST patch is translated along the straight coupling section in 1 μm increments to generate candidate positions P1-P8. The previously identified coarse coupling-region placement is marked as the baseline reference location.

For each placement P_k, the transmission spectrum was computed for both amorphous and crystalline GST states using the same excitation, boundary conditions, and monitor configuration used in the material and coarse location studies. To reflect realistic system constraints in neuromorphic photonic operation, all switching metrics were evaluated under fixed-wavelength readout at $\lambda = 1552.1$ nm, corresponding to the operating wavelength identified from the optimal coarse placement in the angular location study. This approach ensures a consistent comparison across all placements without allowing wavelength retuning.

6.6.2 Evaluation Metrics

To ensure a direct comparison with the material and coarse location studies, the same fixed-wavelength readout procedure and switching metrics are used as defined in Section 6.4.1. In brief, contrast ratio (CR) and modulation depth (MD) are evaluated at the fixed operating wavelength

λ = 1552.1 nm, while linewidth (FWHM) is extracted from the amorphous-state resonance dip and the resonance shift $\Delta\lambda$ is computed from the separation between amorphous and crystalline resonance minima.

6.6.3 Physical Interpretation: Why Fine Positioning Matters

The dependence of switching performance on longitudinal placement can be understood through effective-index perturbation and modal-overlap considerations. For a fixed PCM geometry, the induced change in effective index Δn_{eff} depends on the overlap integral between the guided optical mode and the PCM region. Within the coupling section, the optical field experienced by the resonator is influenced not only by the circulating resonant field but also by the local coupling interaction with the bus waveguide. As a result, the local optical intensity in the resonator waveguide can vary along the coupling length, producing regions where the GST perturbation has amplified influence on the round-trip phase and coupling condition.

Furthermore, because fixed-wavelength switching relies on operating near the steep slope of a resonance feature, even small changes in resonance position or linewidth can change the measured transmission separation between PCM states. Fine positioning along the coupling straight section therefore provides an additional geometric degree of freedom to maximize state-dependent modulation without increasing PCM volume or changing material composition.

6.6.4 Results and Design Implications

The new eight-position coupling-region scan identifies a locally optimal GST placement that improves upon the coarse coupling-region placement defined in the angular location study. In general, positions with stronger modal overlap are expected to yield larger effective perturbations in both refractive index and loss, leading to stronger transmission modulation. However, excessively strong perturbation may also introduce additional optical loss or resonance broadening, potentially reducing spectral selectivity. The optimal position therefore emerges from a trade-off between maximizing CR/MD and preserving resonance sharpness.

In the context of neuromorphic photonic building blocks, this fine optimization is particularly important because it demonstrates that high-performance switching can be achieved through purely geometric tuning of PCM placement, rather than by increasing device footprint, increasing PCM volume, or relying on dynamic nonlinear modeling. The resulting optimal placement from the coupling-region scan is used as the baseline configuration for subsequent analyses and for integration into system-level activation and switching architectures. The transmission spectra for the eight PCM placements are shown in Figures 6.11 and 6.12.

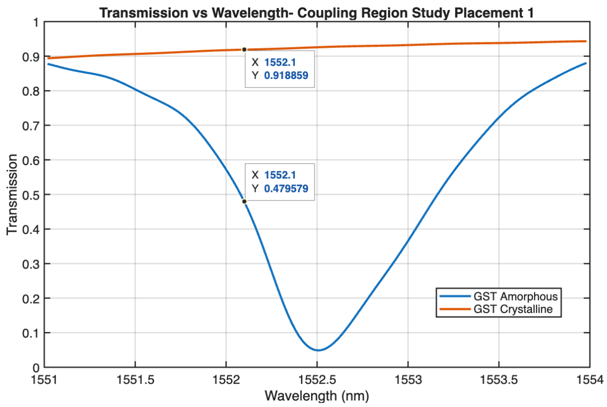

(a) Placement P1

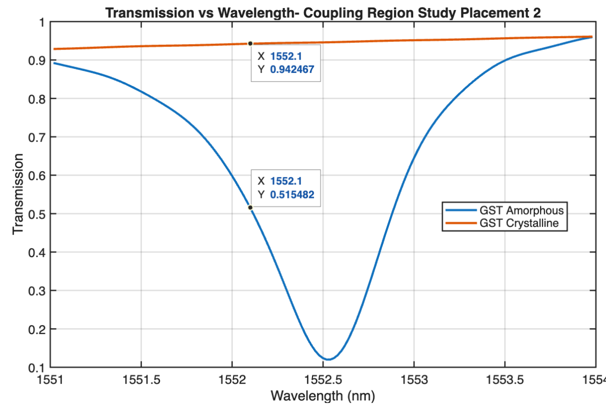

(b) Placement P2

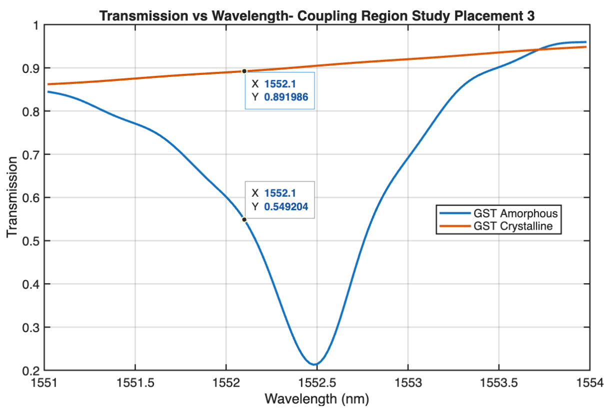

(c) Placement P3

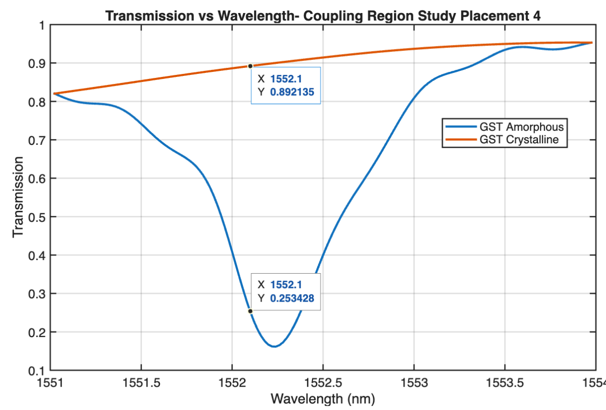

(d) Placement P4

Figure 6.11: Transmission spectra of the GST-integrated racetrack resonator for the first four PCM placements along the coupling region (P1–P4). These positions generally show weaker switching contrast than the baseline, with performance varying non-monotonically along the coupling section.

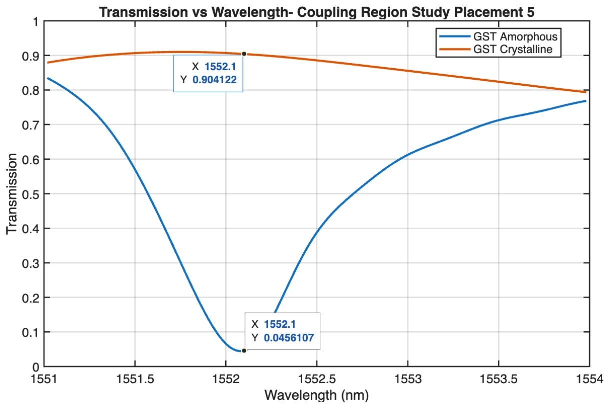

(a) Placement P5

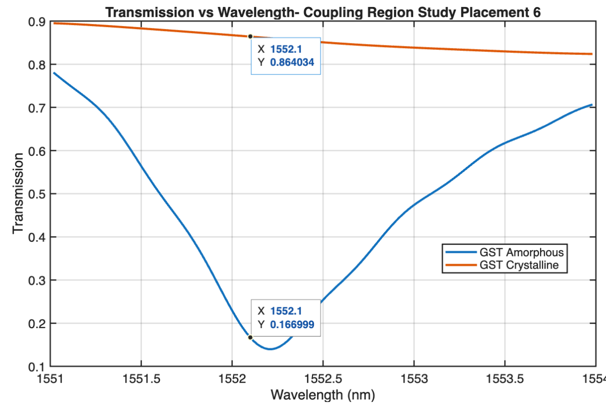

(b) Placement P6

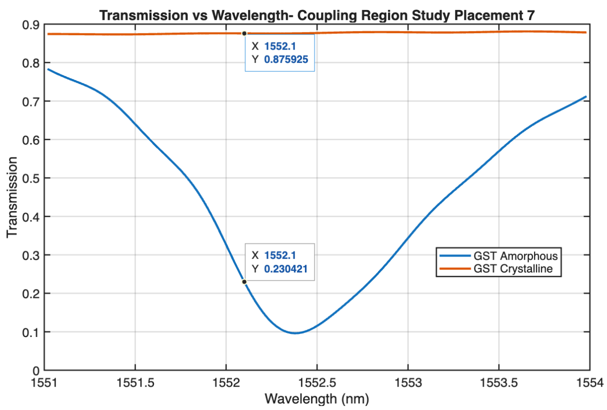

(c) Placement P7

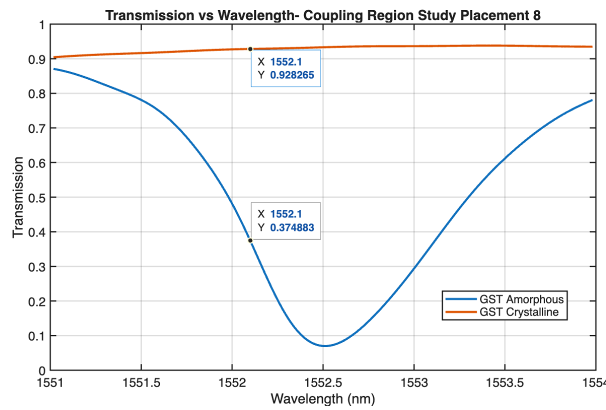

(d) Placement P8

Figure 6.12: Transmission spectra for the remaining PCM placements along the coupling region (P5–P8). Among these positions, P5 produces the highest contrast ratio and modulation depth, indicating that this placement lies closest to the locally optimal balance between modal overlap and resonant perturbation.

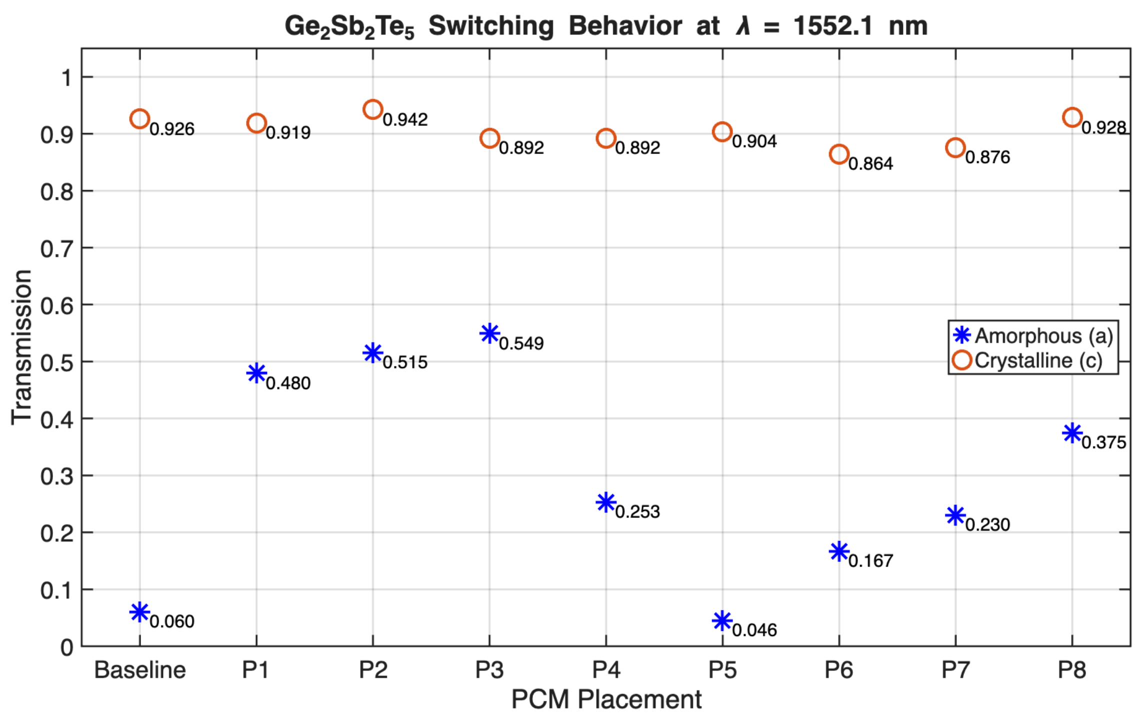

Figure 6.13: Comparison of transmission values for amorphous and crystalline GST states at the fixed operating wavelength $\lambda \approx 1552$ nm for the baseline placement and the eight fine-tuned coupling-region positions. The plot highlights the strong spatial sensitivity of switching performance along the coupling section, with placement P5 providing the lowest amorphous-state transmission and the highest contrast ratio.

Table 6.3: Extracted switching and resonator metrics for the eight GST placements along the coupling region.

Location	**FWHM (nm)**	**CR**	**MD (%)**	**Q**
Baseline	0.42	15.3:1	93.5	3695.5
P1	1.57	1.92:1	47.8	988.60
P2	1.35	1.83:1	45.3	1149.70
P3	1.51	1.62:1	38.4	1027.88
P4	0.89	3.52:1	71.6	1743.93
P5	0.95	19.82:1	94.9	1633.79
P6	1.35	5.17:1	80.7	1149.70
P7	1.58	3.80:1	73.7	982.34
P8	1.69	2.48:1	59.6	918.40

The results of the fine-tuning study summarized in Table 6.3 highlight the trade-offs between resonator quality and switching performance for different GST placements along the coupling region. The baseline configuration corresponds to the optimal placement identified in the preceding location study, where position L1 along the coupling region was determined to provide the most favorable interaction between the optical mode and the PCM. This baseline therefore serves as the reference configuration for the fine-tuning analysis. Among all cases, the baseline placement maintains the narrowest resonance linewidth (FWHM $\approx$ 0.42 nm) and the highest quality factor ($Q \approx 3695$), indicating that this location introduces the least degradation to the resonator while still enabling effective modulation. However, the baseline also produces lower switching contrast compared to another PCM placement. Among the GST-integrated cases, P5 demonstrates the strongest switching performance, achieving the highest contrast ratio ($CR \approx 19.8 : 1$) and modulation depth ($MD \approx 94.9\%$), indicating highly effective optical interaction between the guided mode and the PCM. This improvement in switching contrast comes at the cost of increased optical loss, reflected in the broader resonance (FWHM $\approx$ 0.95 nm) and reduced quality factor ($Q \approx 1633$). In contrast, intermediate placements such as P4 and P6 provide moderate switching performance with improved resonance characteristics compared to positions with very strong perturbation. These placements highlight the trade-off between achieving high transmission contrast and maintaining resonator quality under fixed-wavelength operation. The non-monotonic variation in switching metrics across the coupling region arises from the non-uniform optical field distribution along the coupling section. Since the evaluation is performed at a fixed wavelength, small spatial shifts in PCM placement can significantly alter the alignment between the resonance feature and the operating wavelength, resulting in large variations in transmission contrast and modulation depth even for small positional changes.

6.7 System-Level Activation Modeling Using a Hybrid Opto-Electronic Approach

In neuromorphic photonic systems, nonlinear activation is required to enable tasks such as classification and decision-making. While fully optical nonlinearities are an active area of research, they often require high optical intensities or complex material behavior. For this reason, many practical implementations adopt a hybrid approach, where a linear photonic device is combined with electronic detection and thresholding to achieve nonlinear behavior at the system level.

In this work, the GST-integrated racetrack resonator is designed and simulated as a linear optical device. For a fixed operating wavelength, the transmission of the resonator depends on the phase state of the PCM, resulting in two distinct transmission levels corresponding to the amorphous and crystalline states. Within each state, the response remains linear with respect to the input optical power.

To explore how this device could function within a neuromorphic system, a system-level model was developed in post-processing using MATLAB. The transmission values obtained from Tidy3D simulations were used to compute the output optical power as a function of input power according to

$$P_{\text{out}} = T \cdot P_{\text{in}}, \tag{6.3}$$

where T represents the transmission coefficient for a given PCM state.

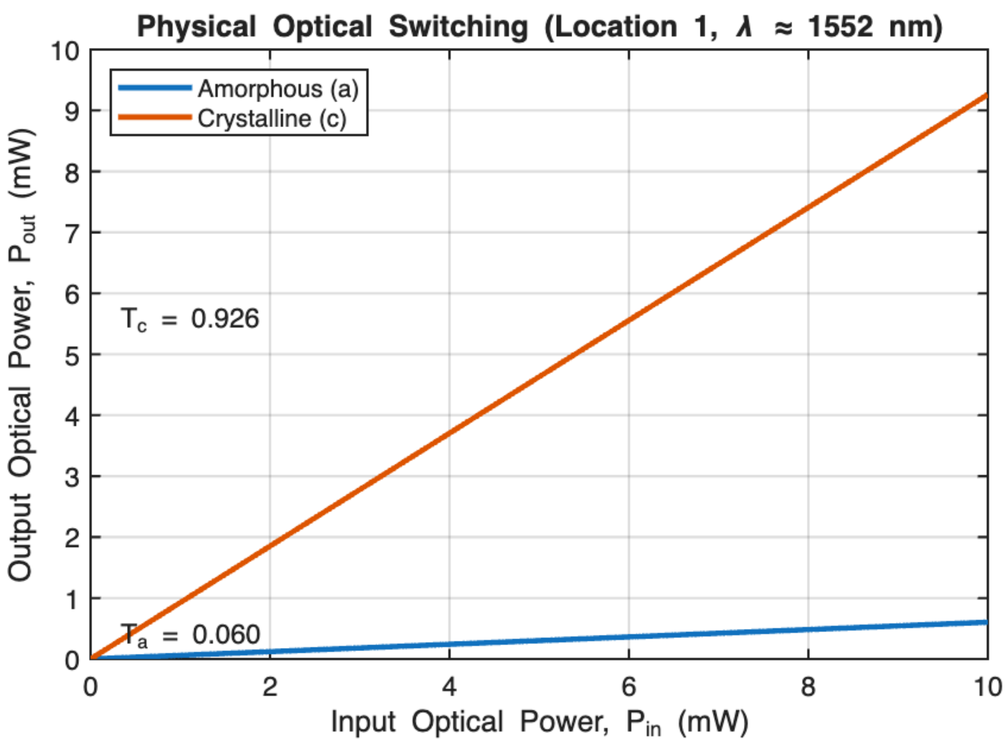

Figure 6.14: Linear optical response of the GST-integrated racetrack resonator at the operating wavelength $\lambda \approx 1552$ nm. The output optical power scales linearly with the input optical power, with distinct slopes corresponding to the amorphous and crystalline PCM states.

This linear optical response represents the photonic front-end of a potential neuron. To emulate a full neuron behavior, the optical signal is conceptually passed through a photodetector and a comparator. The photodetector converts optical power into an electrical signal, and the comparator applies a threshold operation, producing a binary output defined as

$$y = \begin{cases} 0, & V < V_{\text{th}}, \\ 1, & V \geq V_{\text{th}}. \end{cases} \tag{6.4}$$

It is important to note that the photodetection and thresholding stages are not directly simulated in Tidy3D. Instead, they are modeled in MATLAB using the simulated transmission values to evaluate the system-level behavior of the device.

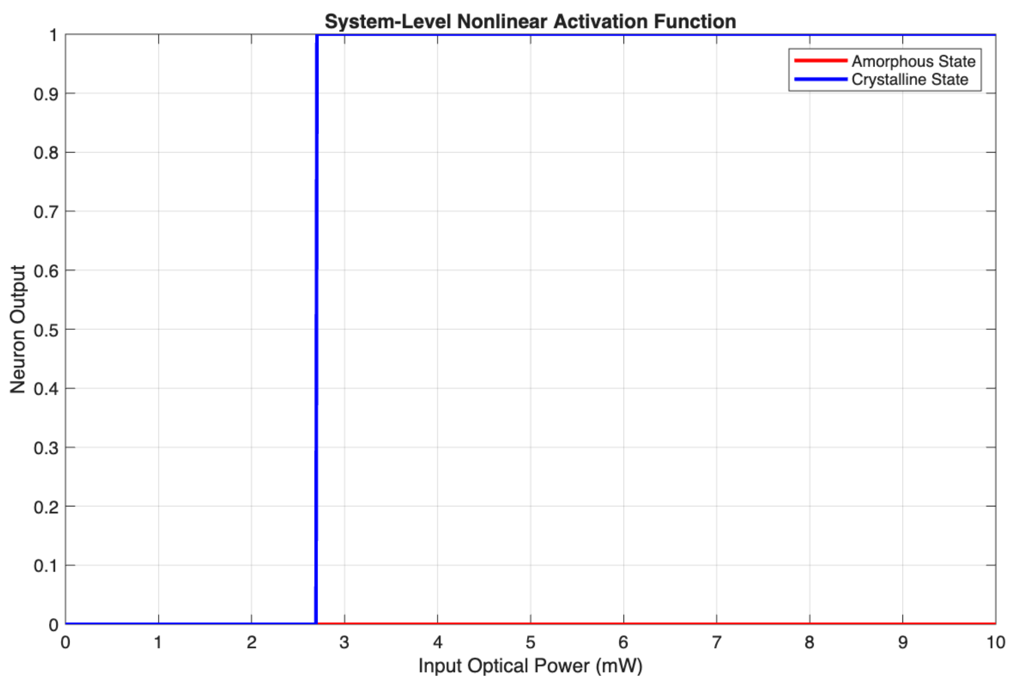

Figure 6.15: System-level activation behavior obtained by applying threshold detection to the linear optical response. The amorphous state remains below threshold due to low transmission, while the crystalline state exceeds the threshold at higher input powers, resulting in a binary switching response.

As shown in Fig. 6.15, the combination of linear optical transmission and electronic thresholding produces a nonlinear, step-like activation response. At low input powers, the output remains in the off state due to insufficient transmitted signal. As the input power increases, only the high-transmission (crystalline) state reaches the threshold, resulting in a transition to the on state. The low-transmission (amorphous) state remains below threshold across the input range.

This result demonstrates that, although the resonator itself is linear, it can serve as an effective front-end for neuron-like activation when combined with standard opto-electronic components. The strong transmission contrast between PCM states enables clear separation between output states, which is essential for reliable signal discrimination in neuromorphic systems.

This hybrid approach provides a practical pathway toward implementing activation functions without relying on intrinsic optical nonlinearities, while still leveraging the advantages of photonic signal processing such as high bandwidth and parallelism.

Chapter 7

Future Work

7.1 Partial Crystallization Modeling

The results presented in this thesis are based on static refractive-index models corresponding to fully amorphous and fully crystalline PCM states. However, experimental studies indicate that practical PCM programming often results in partially crystallized states whose optical properties lie between these two extremes. In particular, Adya et al. reported multilevel resonance tuning in silicon micro-ring modulators arising from incomplete crystallization of the PCM layer, controlled through pulse-width modulation [29]. Such intermediate states arise from non-uniform heating, limited thermal diffusion, or incomplete phase transformation across the PCM volume. Partial crystallization introduces important physical effects that are not captured by binary material models. Spatially non-uniform phase distributions can lead to effective refractive indices that differ from simple volume-weighted averages, while changes in material morphology, such as thinning or reflow during repeated switching, may alter optical loss and mode overlap. Adya et al. observed that partial crystallization could preserve resonance quality while enabling fine-grained tuning, suggesting that intermediate PCM states may be exploited rather than avoided in applications that benefit from analog optical weighting, including neuromorphic photonic systems [29]. Accurately modeling these effects will be essential for predicting state-dependent transfer behavior (or activation-like behavior), modulation depth, and device variability in large-scale photonic neural networks. Future work should therefore incorporate phase-fraction-dependent material models and coupled electro-thermal–optical simulations to capture the dynamics of PCM programming more realistically. Extending the present geometry-driven framework to include partial crystallization modeling would enable exploration of multilevel transfer functions or activation-like responses and analog synaptic behavior, bridging the gap between static resonant switching and fully nonlinear neuromorphic photonic computation. Such extensions would also facilitate closer alignment between simulation results and experimentally demonstrated PCM-based resonator devices.

7.2 Nonlinearity and Path Toward Nonlinear Optical Switching

The racetrack resonators investigated in this thesis operate through state-dependent refractive index modulation of PCMs. The demonstrated switching behavior arises from controlled shifts in the resonance condition caused by changes in the effective refractive index, as described in Chapter 3. While this mechanism produces strong transmission contrast between material states, each programmed state remains optically linear under low-power readout conditions. Therefore, the present work establishes a geometry-optimized resonant switching platform rather than a fully intensity-dependent nonlinear optical activation function.

Achieving intrinsic optical nonlinearity would require the device transmission to depend directly on input optical intensity. In resonator-based systems, such nonlinear behavior can arise from intensity-dependent refractive index changes, free-carrier dispersion, two-photon absorption, or thermo-optic effects [21, 24]. In silicon photonics, the dominant nonlinear mechanism at telecommunications wavelengths is the third-order susceptibility ($\chi^{(3)}$), which gives rise to the Kerr effect. Under sufficiently high optical intensities, the refractive index becomes power-dependent, modifying the resonance condition dynamically and enabling phenomena such as bistability and nonlinear resonance distortion [9, 21].

High-quality-factor (Q) whispering gallery mode resonators are particularly attractive for nonlinear operation because circulating optical power inside the cavity can exceed the input power by several orders of magnitude [23]. This field enhancement effectively lowers the threshold required to observe nonlinear effects. Extending the racetrack geometries developed in this thesis to operate in a higher optical power regime may therefore enable measurable Kerr-induced resonance shifts or hysteretic transmission behavior.

A second pathway toward nonlinearity involves exploiting the threshold-dependent phase-transition dynamics of PCMs themselves. Unlike purely linear refractive-index tuning, phase transitions in materials such as GST are inherently nonlinear processes governed by energy density and thermal dynamics [13, 14]. When the deposited optical or electrical energy exceeds a critical threshold, rapid crystallization or amorphization occurs. Below this threshold, minimal structural change is observed. If optical power alone is used to induce phase transitions within the resonator, the transmission response could become intensity-dependent, forming a true nonlinear optical switching mechanism.

Furthermore, partial crystallization introduces an additional opportunity for nonlinear behavior. Experimental studies have demonstrated multilevel resonance tuning arising from intermediate crystallization states controlled through pulse energy modulation [29]. If the effective refractive index depends nonlinearly on deposited energy or optical intensity, the resulting transmission curve may exhibit activation-like characteristics similar to those required in neuromorphic architectures

[4, 20]. In this context, the racetrack resonator would transition from a binary programmable element to a continuously tunable, intensity-responsive activation node.

Importantly, the geometry-driven sensitivity demonstrated in this thesis provides a strong foundation for such nonlinear extensions. By strategically positioning PCM segments near high-field or coupling regions, the overlap between the optical mode and the perturbing material is maximized. This enhancement increases the effective index change per unit material volume, thereby reducing the optical energy required to induce measurable resonance shifts. In other words, geometric optimization serves as a mechanism for lowering nonlinear switching thresholds.

Future work should therefore explore three complementary directions:

1. **High-Intensity Resonant Operation:** Characterizing Kerr-induced and free-carrier-induced nonlinear resonance shifts in racetrack geometries under elevated optical power.

2. **Coupled Electro-Thermal-Optical Modeling:** Incorporating thermal diffusion and phase-transition dynamics into full-wave simulations to predict optically driven PCM switching behavior.

3. **Hybrid Opto-Electronic Activation:** Integrating the linear photonic core demonstrated in this thesis with electronic threshold circuits, as proposed in neuromorphic photonic architectures [20], to implement nonlinear activation externally while preserving low-loss optical summation.

Ultimately, transitioning from geometry-optimized resonant switching to fully nonlinear optical activation will require combining electromagnetic field enhancement with material dynamics and thermal engineering. The racetrack platform developed in this work provides the structural flexibility and sensitivity necessary to enable that transition. Rather than viewing the absence of intrinsic nonlinearity as a limitation, this thesis establishes the physical groundwork upon which nonlinear photonic activation mechanisms can be systematically realized and optimized for scalable neuromorphic hardware.

Chapter 8

Discussion and Conclusion

This thesis investigated the design and optimization of a phase-change-material integrated silicon racetrack microresonator for nonvolatile optical switching in neuromorphic photonic systems. The work focused on understanding how both material selection and spatial placement of the PCM influence resonant transmission behavior under fixed-wavelength optical readout. By combining electromagnetic theory, numerical simulation, and systematic design exploration, the study established a geometry-driven framework for optimizing resonator-based photonic switching elements that can serve as building blocks for neuromorphic photonic hardware.

The motivation for this work arises from the growing need for scalable computing platforms capable of supporting artificial intelligence workloads with improved energy efficiency and bandwidth. As discussed in earlier chapters, conventional electronic architectures suffer from the von Neumann bottleneck, where the separation of memory and processing leads to excessive data movement and power consumption. Photonic systems offer a potential pathway toward overcoming these limitations due to their intrinsic parallelism, high bandwidth, and low propagation loss. However, practical neuromorphic photonic hardware requires compact device-level primitives capable of providing programmable transmission states, memory retention, and nonlinear activation behavior. Resonator-based devices integrated with phase-change materials represent one promising approach toward achieving these capabilities.

The first step in this work was the development of a baseline racetrack resonator design suitable for operation near the telecommunications wavelength of 1.55 μm. Using three-dimensional finite-difference time-domain simulations, the intrinsic transmission response of the silicon racetrack resonator was characterized in the absence of PCM perturbations. This baseline analysis confirmed the presence of a well-defined resonance dip with a narrow linewidth, establishing a reference point for evaluating switching behavior after PCM integration. The racetrack geometry was selected because its straight coupling sections provide additional design flexibility compared to conventional microring resonators, allowing systematic study of spatial material placement effects.

Following the baseline characterization, a comparative material study was conducted to evaluate three candidate phase-change materials: Sb_2S_3, Sb_2Se_3, and GST. Each material was integrated into the same racetrack geometry at the waveguide-resonator coupling region and simulated in both amorphous and crystalline states using experimentally reported optical constants. The results revealed clear differences in switching behavior among the materials. While Sb_2S_3 and Sb_2Se_3 produced measurable resonance modulation, both materials exhibited either limited transmission contrast or significant resonance shifts that reduced switching performance under fixed-wavelength operation. In contrast, GST demonstrated strong state-dependent transmission separation while maintaining resonance stability and relatively narrow linewidth. These characteristics resulted in the highest contrast ratio and modulation depth among the tested materials, leading to its selection as the optimal PCM for the remainder of the study.

With the PCM material fixed, the next stage of the investigation focused on understanding how spatial placement of the GST segment influences switching behavior. Because optical field intensity and phase sensitivity vary along the resonator perimeter, identical PCM segments positioned at different locations can produce significantly different resonant responses. To quantify this effect, a location study was performed in which the GST segment was rotated around the racetrack in four 90° increments. The results showed a clear dependence of switching performance on PCM placement. When the GST segment was positioned at the waveguide–resonator coupling region, the device exhibited the strongest transmission modulation, highest contrast ratio, and narrowest resonance linewidth. As the PCM segment was moved away from this region, both modulation depth and spectral selectivity degraded. This behavior is consistent with the stronger optical field interaction and enhanced phase sensitivity present near the coupling interface.

To further refine this observation, a fine-resolution scan was performed along the straight coupling section of the racetrack resonator. In this study, the GST segment was translated longitudinally across the coupling region in multiple discrete positions while keeping all other parameters fixed. This fine placement study revealed that switching performance varies significantly even within the same coupling section. Among the tested positions, one configuration (denoted P5) produced the highest contrast ratio and modulation depth while maintaining acceptable resonance characteristics. This result demonstrates that local modal overlap and resonant field distribution play a critical role in determining the effective index perturbation induced by the PCM. Importantly, this improvement was achieved through purely geometric optimization, without increasing PCM volume or altering material composition.

Taken together, the results of the material, angular placement, and fine-position studies establish a clear design methodology for optimizing PCM-integrated resonant photonic switches. First, the PCM material must provide strong refractive index contrast while maintaining manageable optical loss. Second, the PCM should be positioned near regions of high optical field sensitivity, particularly the coupling interface of the resonator. Third, fine-scale positioning within that region can further enhance switching performance by maximizing modal overlap with the circulating optical field. These findings demonstrate that geometric design parameters play an equally important role as material properties in determining the effectiveness of PCM-integrated photonic devices.

Beyond device-level switching, the thesis also explored how the optimized resonator can function as a component within a neuromorphic photonic architecture. While the PCM-induced modulation demonstrated in this work remains optically linear within each programmed state, nonlinear activation behavior can be realized at the system level through hybrid opto-electronic integration. In this architecture, the racetrack resonator provides a linear photonic transmission response that depends on the PCM state, while photodetection and electronic thresholding introduce the nonlinear decision function required for neuron-like behavior. This hybrid approach allows the photonic device to perform high-speed optical signal processing while relying on mature electronic circuits to implement activation functions.

From a broader perspective, the results presented in this thesis highlight the importance of device-level optimization in enabling scalable photonic computing systems. Neuromorphic photonic architectures rely on large numbers of interconnected optical components, where small improvements in device efficiency, contrast, or footprint can significantly influence overall system performance. The geometry-driven optimization strategy demonstrated here provides a systematic approach for improving switching behavior without introducing additional complexity or power consumption.

It is important to note that the present study focused on static refractive-index models corresponding to fully amorphous and fully crystalline PCM states. Dynamic phase transitions, partial crystallization effects, and thermal dynamics were not included in the electromagnetic simulations. While this simplified modeling approach enabled clear isolation of geometry-driven switching mechanisms, incorporating more realistic material dynamics will be necessary to fully capture the behavior of PCM-integrated devices under practical operating conditions. Such extensions represent an important direction for future research.

Despite these limitations, the results of this thesis demonstrate that PCM-integrated racetrack resonators can provide strong, nonvolatile transmission modulation with compact device footprints and favorable spectral characteristics. The optimized configurations identified in this work achieve high contrast ratios and modulation depths while maintaining narrow resonance linewidths, making them suitable candidates for resonant switching elements in integrated photonic circuits.

In conclusion, this thesis establishes a systematic design framework for phase-change-material-integrated racetrack resonators intended for neuromorphic photonic hardware. Through comparative material analysis, spatial placement studies, and fine geometric optimization, the work demonstrates that both material properties and resonator geometry critically influence switching performance. The findings provide practical design guidelines for developing compact, programmable photonic switching elements and lay the groundwork for future extensions incorporating nonlinear optical dynamics, multilevel PCM states, and fully integrated photonic neural networks.

References

[1] T. Y. Teo, M. Krbal, J. Mistrik, J. Prikryl, L. Lu, and R. E. Simpson, "Comparison and analysis of phase change materials-based reconfigurable silicon photonic directional couplers," *Opt. Mater. Express*, vol. 12, pp. 606–621, 02 2022.

[2] R. Sweiss, S. J. Mishu, Y. M. Banad, and S. Sharif, "Nonvolatile linear resonant switching for neuromorphic photonics in a pcm-integrated silicon racetrack microresonator," in *Proc. SPIE 13901, Smart Photonic and Optoelectronic Integrated Circuits 2026*, vol. 13901, 2026, p. 139010D.

[3] F. Inc., "Tidy3d electromagnetic solver," https://www.flexcompute.com/tidy3d/, 2024, accessed 2026.

[4] P. R. Prucnal and B. J. Shastri, *Neuromorphic photonics*. CRC press, 2017.

[5] M. A. Nahmias, B. J. Shastri, A. N. Tait, T. Ferreira de Lima, and P. R. Prucnal, "Neuromorphic photonics," *Optics and Photonics News*, vol. 29, no. 1, pp. 34–41, 2018.

[6] B. J. Shastri, A. N. Tait, T. Ferreira de Lima, W. H. Pernice, H. Bhaskaran, C. D. Wright, and P. R. Prucnal, "Photonics for artificial intelligence and neuromorphic computing," *Nature Photonics*, vol. 15, no. 2, pp. 102–114, 2021.

[7] J. Feldmann, N. Youngblood, C. D. Wright, H. Bhaskaran, and W. H. Pernice, "All-optical spiking neurosynaptic networks with self-learning capabilities," *Nature*, vol. 569, no. 7755, pp. 208–214, 2019.

[8] S. S. Sharif, H. Karimkhani, and Y. M. Banad, "Exploring nonlinear activation function within microring resonators for all-photonic neuromorphic computing," in *Physics and Simulation of Optoelectronic Devices XXXII*, vol. 12880. SPIE, 2024, pp. 189–193.

[9] W. Bogaerts, P. D. Heyn, T. V. Vaerenbergh, K. D. Vos, S. K. Selvaraja, T. Claes, P. Dumon, P. Bienstman, D. V. Thourhout, and R. Baets, "Silicon microring resonators," *Laser & Photonics Reviews*, vol. 6, no. 1, pp. 47–73, 2012.

[10] Z. Fu, Z. Wang, P. Bienstman, R. Jiang, J. Wang, and C. Wu, "Programmable low-power consumption all-optical nonlinear activation functions using a micro-ring resonator with phase-change materials," *Optics Express*, vol. 30, no. 25, pp. 44 943–44 953, 2022.

[11] M. Rudé, J. Pello, R. E. Simpson, J. Osmond, G. Roelkens, J. J. G. M. van der Tol, and V. Pruneri, "Optical switching at 1.55 μm in silicon racetrack resonators using phase-change materials," *Applied Physics Letters*, vol. 103, no. 14, p. 141119, 2013.

[12] Z. Zhang, J. Li, G. Wang, Z. Shang, H. Chen, Z. Zhao, M. Zhang, F. Liu, B. Dong, K. Guo, and P. Yan, "Racetrack resonator based integrated phase shifters on silicon nitride platform," *Infrared Physics & Technology*, vol. 125, p. 104276, 2022.

[13] M. Wuttig, H. Bhaskaran, and T. Taubner, "Phase-change materials for non-volatile photonic applications," *Nature Photonics*, vol. 11, pp. 465–476, 2017.

[14] S. Abdollahramezani, O. Hemmatyar, H. Taghinejad, A. Krasnok, Y. Kiarashinejad, M. Zandehshahvar, A. Alù, and A. Adibi, "Tunable nanophotonics enabled by chalcogenide phase-change materials," *Nanophotonics*, vol. 9, no. 5, pp. 1189–1241, 2020.

[15] I. Chakraborty, G. Saha, A. Sengupta, and K. Roy, "Toward fast neural computing using all-photonic phase change spiking neurons," *Scientific Reports*, vol. 8, p. 12980, 2018.

[16] W. H. P. Pernice and H. Bhaskaran, "Photonic non-volatile memories using phase change materials," *Applied Physics Letters*, vol. 101, no. 17, p. 171101, 2012.

[17] K. J. Miller, R. F. Haglund, and S. M. Weiss, "Optical phase change materials in integrated silicon photonic devices: review," *Optical Materials Express*, vol. 8, no. 8, pp. 2415–2429, 2018.

[18] J. Feldmann, N. Youngblood, M. Karpov, H. Gehring, X. Li, M. Stappers, M. Le Gallo, X. Fu, A. Lukashchuk, A. S. Raja *et al.*, "Parallel convolutional processing using an integrated photonic tensor core," *Nature*, vol. 589, no. 7840, pp. 52–58, 2021.

[19] D. Marković, A. Mizrahi, D. Querlioz, and J. Grollier, "Physics for neuromorphic computing," *Nature Reviews Physics*, vol. 2, pp. 499–510, 2020.

[20] B. J. Shastri, A. N. Tait, T. Ferreira de Lima, W. H. P. Pernice, H. Bhaskaran, C. D. Wright, and P. R. Prucnal, "Photonics for artificial intelligence and neuromorphic computing," *Nature Photonics*, vol. 15, no. 2, pp. 102–114, 2021.

[21] R. W. Boyd, *Nonlinear Optics*, 3rd ed. Academic Press, 2008.

[22] M. Wuttig and N. Yamada, “Phase-change materials for rewriteable data storage,” *Nature Materials*, vol. 6, pp. 824–832, 2007.

[23] K. J. Vahala, “Optical microcavities,” *Nature*, vol. 424, pp. 839–846, 2003.

[24] R. A. Soref, “The past, present, and future of silicon photonics,” *IEEE Journal of Selected Topics in Quantum Electronics*, vol. 12, no. 6, pp. 1678–1687, 2006.

[25] D. Thomson, A. Zilkie, J. E. Bowers, T. Komljenovic, G. T. Reed, L. Vivien, D. Marris-Morini, E. Cassan, L. Virot, J.-M. Fédéli *et al.*, “Roadmap on silicon photonics,” *Journal of Optics*, vol. 18, no. 7, p. 073003, 2016.

[26] J. D. Jackson, *Classical Electrodynamics*, 3rd ed. Wiley, 1999.

[27] B. E. A. Saleh and M. C. Teich, *Fundamentals of Photonics*, 3rd ed. Wiley, 2019.

[28] J. D. Joannopoulos, S. G. Johnson, J. N. Winn, and R. D. Meade, *Photonic Crystals: Molding the Flow of Light*, 2nd ed. Princeton University Press, 2008.

[29] U. Adya, S. Singhal, R. Chen *et al.*, “Non-volatile tuning of cryogenic silicon photonic micro-ring modulators,” *Nature Communications*, vol. 16, p. 9290, 2025.

[30] P. Dumon, W. Bogaerts, V. Wiaux, J. Wouters, S. Beckx, J. Van Campenhout, D. Taillaert, B. Luyssaert, P. Bienstman, D. Van Thourhout, and R. Baets, “Low-loss soi photonic wires and ring resonators fabricated with deep uv lithography,” *IEEE Photonics Technology Letters*, vol. 16, no. 5, pp. 1328–1330, 2004.

[31] T. Li, Y. Li, Y. Wang, Y. Liu, Y. Liu, Z. Wang, R. Miao, D. Han, Z.-Q. Hui, and W. Li, “Neuromorphic photonics based on phase change materials,” *Nanomaterials*, vol. 13, p. 1756, 05 2023.